nature communications

Article

https://doi.org/10.1038/s41467-026-70153-4

Single-cell transcriptomics reveals hair growth retardation mediated by aberrant connective tissue sheath contraction in male androgenetic alopecia

Received: 19 August 2024

Accepted: 19 February 2026

Published online: 26 February 2026

Check for updates

Guo Li[1,2,3,4,8], Li Yang[1,2,3,4,8], Shixin Duan[1,2,3,4,8], Mengting Chen[1,2,3,4], Yujin Zhang[5], Fangfen Liu[1,2,3,4], Yunying Wang[1,2,3,4,6], Jiayun Li[1,2,3,4], San Xu[1,2,3,4], Zheng Wu[1,2,3,4], Mei Wang[1,2,3,4], Ben Wang[1,2,3,4], Zhixiang Zhao[1,2,3,4], Wei Shi[1,2,3,4], Mingxing Lei[7], Hongfu Xie[1,2,3,4], Yan Tang[1,2,3,4] ✉, Zhili Deng[1,2,3,4] ✉ & Ji Li[1,2,3,4] ✉

Androgenetic alopecia (AGA) manifests as progressive hair follicle (HF) miniaturization; however, its drivers remain poorly elucidated. Combining spatial and single-cell transcriptomics, we generate a concise single-cell atlas of anagen HFs in male AGA, revealing early changes in cell subpopulations, altered HF stem cell fate determination, and disrupted cell-cell communications. Through ex vivo HF organ culture and humanized mouse models, we demonstrate that hypercontractility of connective tissue sheath (CTS) activates the mechanosensitive channel PIEZO1 in anagen HFs. This mechanotransduction induces ectopic apoptosis of HF progenitor cells and suppresses matrix/ORS cell proliferation, depleting progenitor pools and impairing HF growth, thereby driving progressive miniaturization. Critically, pharmacological inhibition of CTS contraction via ML-7, a selective myosin light chain kinase (MLCK) inhibitor, improves HF growth in both male AGA patient-derived ex vivo models and humanized mice. Our study delineates the cellular dynamics underlying male AGA pathogenesis and identifies mechanopathologically activated CTS as a key driver of HF miniaturization, positioning the peri-follicular CTS as a promising therapeutic target for AGA intervention.

Androgenetic alopecia (AGA), also known as male pattern baldness, is the most common type of hair loss, affecting both men and women. Although existing evidence suggests that androgen signaling pathways may play important roles in AGA pathogenesis[1–5], the precise mechanisms underlying its development remain largely unknown. AGA incidence increases with age, with over 50% of Caucasian males affected by age 50[6,7]. Its profound psychosocial impact drives strong treatment-seeking behaviors, particularly among females and young males[8–12]. Despite this clinical urgency, therapeutic development remains constrained by limited pathophysiological understanding. Currently, only two therapies (oral finasteride and topical minoxidil) have been approved by the Food and Drug Administration (FDA), both carrying persistent safety concerns[13–18]. This underscores the critical need to systematically characterize the pathogenic regulatory networks underlying AGA for developing mechanism-driven therapeutic interventions.

A full list of affiliations appears at the end of the paper. ✉e-mail: ytang_xy@csu.edu.cn; dengzhili@csu.edu.cn; liji_xy@csu.edu.cn

AGA pathogenesis is characterized by progressive and patterned conversion of large terminal hair follicles (HFs) into small vellus-like structures (termed as HF miniaturization) through dysregulated cycling dynamics[19,20]. All HFs undergo periodic cycles of growth (anagen), regression (catagen), and rest (telogen) stages throughout the lifetime[21–23]. While normal human HFs maintain prolonged anagen phases (2–6 years) to sustain robust hair growth, AGA-affected HFs exhibit truncated anagen duration with premature catagen entry and prolonged telogen. These perturbations lead to diminished HF size, reduced hair shaft diameter and decreased anagen/telogen ratios, culminating in microscopic hairs characteristic of balding scalps as the HF cycles[24–26]. In HF cycle, the growth of HFs primarily relies on interactions between the rapidly proliferating hair matrix cells and the components of the niche (including dermal papilla (DP), dermal sheath (DS), fibroblasts, adipocytes and blood vessels, etc.)[19,27–32]. Crucially, although HF stem cells (HFSCs) persist in AGA-affected bulges, their activated progenitor cell progeny—essential for fueling the matrix cell pool—become depleted[33,34]. This creates an unresolved paradox: preserved stem cell reservoirs coexisting with insufficient regenerative capacity.

Current AGA research remains constrained by methodological limitations. Histomorphological analyses and bulk transcriptomic approaches fail to capture cellular heterogeneity, while existing animal models inadequately recapitulate human AGA pathology[6,13,35]. Emerging single-cell RNA-sequencing (scRNA-seq) and spatial transcriptomics technologies offer unprecedented resolution for deconstructing cellular dynamics, lineage trajectories, and niche interactions in complex tissues[36–40]. Nevertheless, these cutting-edge tools have yet to be applied to systematically investigate AGA pathogenesis.

In this study, we integrate scRNA-seq with spatial transcriptomics to construct the first cellular atlas of human anagen HFs in male AGA, revealing early pathogenic alterations in cellular hierarchies and communication networks. Through synergistic use of ex vivo HF organ culture models and humanized mouse models, we identify hypercontractility of the connective tissue sheath (CTS) as a mechanopathological driver of HF miniaturization. Our findings not only elucidate CTS-mediated mechanotransduction pathways impairing HF growth, but also demonstrate therapeutic efficacy through targeted CTS relaxation—providing a paradigm-shifting strategy for AGA treatment.

Results

Single-cell and spatial transcriptomics reveals cell heterogeneity of male androgenetic alopecia and healthy anagen HF units

To dissect the cellular heterogeneity and explore the early changes in AGA development, we obtained anagen HF units of both frontal balding (B) scalps and occipital non-balding (NB) scalps from the same male AGA patients ($n = 4$), and frontal normal scalps of healthy male volunteers (HS, $n = 4$), to perform scRNA-seq; and acquired a normal frontal scalp containing anagen HFs from one healthy male volunteer to perform spatial transcriptomics (Stereo-seq) (Fig. 1a). Among these, anagen HFs of balding scalps were at the early stage of hair miniaturization, isolated from the edge of frontal hairline of male AGA patients. Prior to scRNA-seq and Stereo-seq profiling, we implemented a multimodal verification strategy to confirm anagen phase status in human HFs, adapting established methodologies for hair cycle staging[41–43]. Our results showed that compared to catagen HFs, anagen HFs exhibited hair matrix (HM) with larger volume, more onion-shaped DP and maximal melanin content; besides, the HM cells displayed obvious proliferative activity and no apoptotic signals (Fig. S1). After sequencing and stringent cell filtration of scRNA-seq data, 76368 cells were retained for subsequent analyses (Supplementary Data 1). Following a standard scRNA-seq data analysis procedure, totally 28 clusters (C0-C27) were retained, which were sufficiently separated from each other (Fig. S2a), and these clusters could be reproduced using cells from each of the 12 samples, suggesting that they are robustly present across different samples and conditions (including HS, NB and B) (Fig. S2b, c).

To dissect the cell types, we first defined the expression pattern of SOX9 (Fig. S2d), a reported marker for hair follicle cells[44]. By immunohistochemistry, we confirmed that SOX9 is expressed in most cells of hair follicle and almost none in other cells, distinguishing hair follicle cells from other epidermal and dermal cells (Fig. S2e). Based on the expression of SOX9 and known lineage markers, the above clusters were preliminarily identified as the following different cell types, including Bulge ($KRT15^+/CXCL14^+$), DP ($VCAN^+/CFD^+$), DS ($ACTA2^+/CCN2^+$), outer root sheat suprabasal (ORS SB; $KRT6A^+/SOX9^+$), matrix ($MKI67^+/SOX9^+$), endothelial cells (Endo; $PECAM1^+/VWF^+$), immune cells ($CD3D^+$), Langerhans ($CD207^+/CD1A^+$), Melanocytes ($DCT^+/MLANA^+$), Vascular smooth muscle cells/pericytes (vSMCs; $ACTA2^+/MYH11^+/TAGLN^+$), sebaceous gland cells (DCD^+/SCD^+), sweet gland cells (SwGs; $KRT8^+/KRT18^+$), sweet gland duct cells (SGDCs; $KRT77^+$), interfollicular epidermis spinous (IFE spinous; $KRT1^+/KRT10^+$), IFE granular ($FLG^+/KRT2^+$), IFE proliferative ($KRT10^+/MKI67^+$); cells highly expressing KRT14 but not SOX9 were defined as IFE basal[45–56] (Fig. 1b, c; Supplementary Data 2 and Fig. S2f–m). To resolve the ambiguities of cell clustering in scRNA-seq analyses, we projected single-cell annotations onto Stereo-seq spatial maps and refined cluster classifications using spatial localization patterns. This integrative analysis not only confirmed the accuracy of our original single-cell clustering but also enabled definitive identification of previously ambiguous populations: ORS basal ($S100A2^+$), inner infundibulum/isthmus cells (Inner II; $S100A8^+/S100A9^+$), and Outer II ($SEMA5A^+/PTN^+$) (Fig. 1b–e; Supplementary Data 2, 3 and Fig. S3a, b). Significantly, spatial transcriptomics uncovered the inner root sheath (IRS) population with high TCHH expression—undetectable in single-cell datasets (Fig. S3b, c).

Consistent with the scRNA-seq and Stereo-seq data, immunostaining analysis showed that KRT15 was highly expressed in bulge HFSCs and moderately expressed in IFE basal cells (Fig. 1f), similar to previous observations[33,46]. As an ORS marker, KRT6A was exactly expressed mainly in the ORS SB and some of the inner layer cells of the infundibulum and isthmus, which are the upward continuation of ORS (Fig .1g and Fig. S4a). Moreover, we verified IFE spinous cells with KRT10, and DS cells with α-SMA and CCN2 (Fig. 1h, i). We determined the relative proportion of each HF cell type in all samples, showing increased outer II cells, and slightly decreased ORS basal cells in B anagen HF units compared with NB or HS (Fig. S4b; Supplementary Data 4). We next explored the molecular changes in each cell type of balding HF unit compared to that of NB/HS group (including differentially expressed genes (DEGs), and enriched pathways). Our results uncovered a landscape of transcriptional dysregulation across all major cell types in AGA anagen HFs (Fig. S4c and Supplementary Data 5, 6). Notably, HFSCs exhibited a pronounced inflammatory signature, characterized by upregulation of pro-inflammatory pathways such as TNF signaling, concomitant with a downregulation of pathway governing organ growth. DP cells, the signaling orchestrators of HF regeneration, showed a marked suppression of angiogenesis-related pathways, suggesting a compromised microvascular niche. Matrix cells, which are directly responsible for hair shaft production, were ensnared in a pro-inflammatory milieu, as evidenced by the significant upregulation of cytokine-cytokine receptor interaction. The complete datasets of differential gene expression, and upregulated or downregulated pathways for all cell types is available in Supplementary Data 5 and 6.

To further explore the potential heterogeneity, HFSCs (bulge cells) were subclustered into three distinct subclusters (Fig. 2a), in which the percentage of subcluster 1 was reduced in the balding bulge of AGA patients (Fig. 2b). Wilcoxon rank-sum test was used to characterize the marker genes specifically enriched in each subpopulation

https://doi.org/10.1038/s41467-026-70153-4

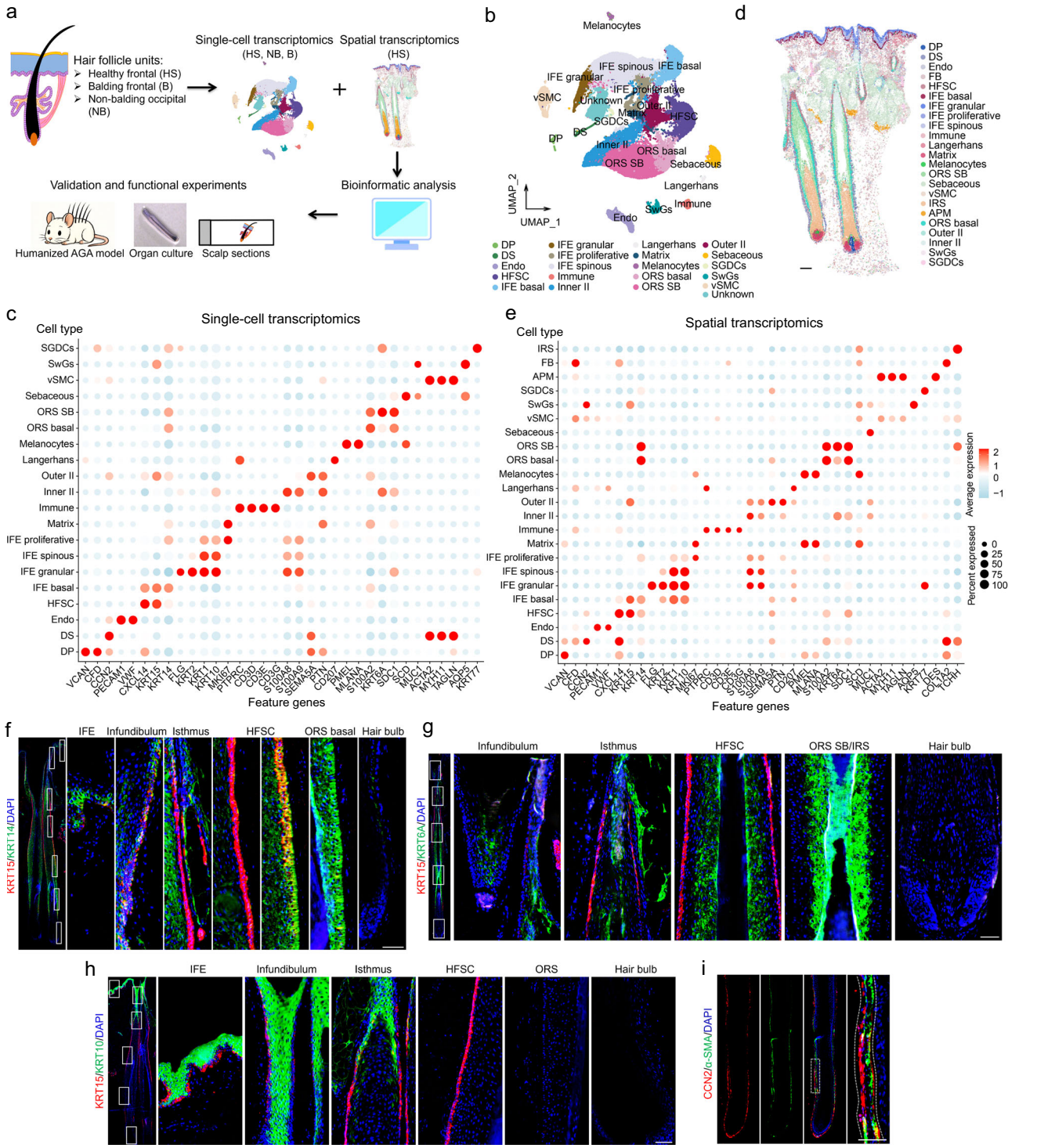

Fig. 1 | Single-cell and spatial transcriptomics reveal cell type composition in anagen hair follicle units of androgenetic alopecia and healthy scalps. **a** Workflow overview of single-cell and spatial transcriptomics, followed by validation and functional experiments using anagen hair follicles (HFs) from balding frontal (B) and non-balding (NB) occipital scalps of androgenetic alopecia (AGA) patients, and from normal scalps of healthy individuals (HS). **b** Uniform manifold approximation and projection (UMAP) plot showing 21 cell types identified in human anagen hair follicles. Dermal papilla (DP), dermal sheath (DS), endothelial cells (Endo), hair follicle stem cells (HFSC), interfollicular epidermis (IFE), inner layer of infundibulum and isthmus (Inner II), outer root sheath basal (ORS basal), outer root sheath suprabasal (ORS SB), outer layer of infundibulum and isthmus (Outer II), sweat gland cells (SwGs), sweat gland duct cells (SGDCs), and vascular smooth muscle cells (vSMC) are indicated. **c** Dot plot showing expression of representative marker genes for each cell type identified by single-cell RNA sequencing. **d** Cell-type spatial map of normal frontal scalp from a healthy male volunteer generated by spatial transcriptomics. Scale bar, 200 μm. **e** Dot plot showing expression of marker genes for each cell type identified by spatial transcriptomics. **f**–**i** Representative immunostaining images of KRT15/KRT14 (**f**) KRT6A/KRT15 (**g**) KRT15/KRT10 (**h**) and α-smooth muscle actin/CCN2 (**i**) in human scalp sections, with magnified views of boxed regions. $n = 5$ HFs from 3 independent individuals. Scale bar, 50 μm.

https://doi.org/10.1038/s41467-026-70153-4

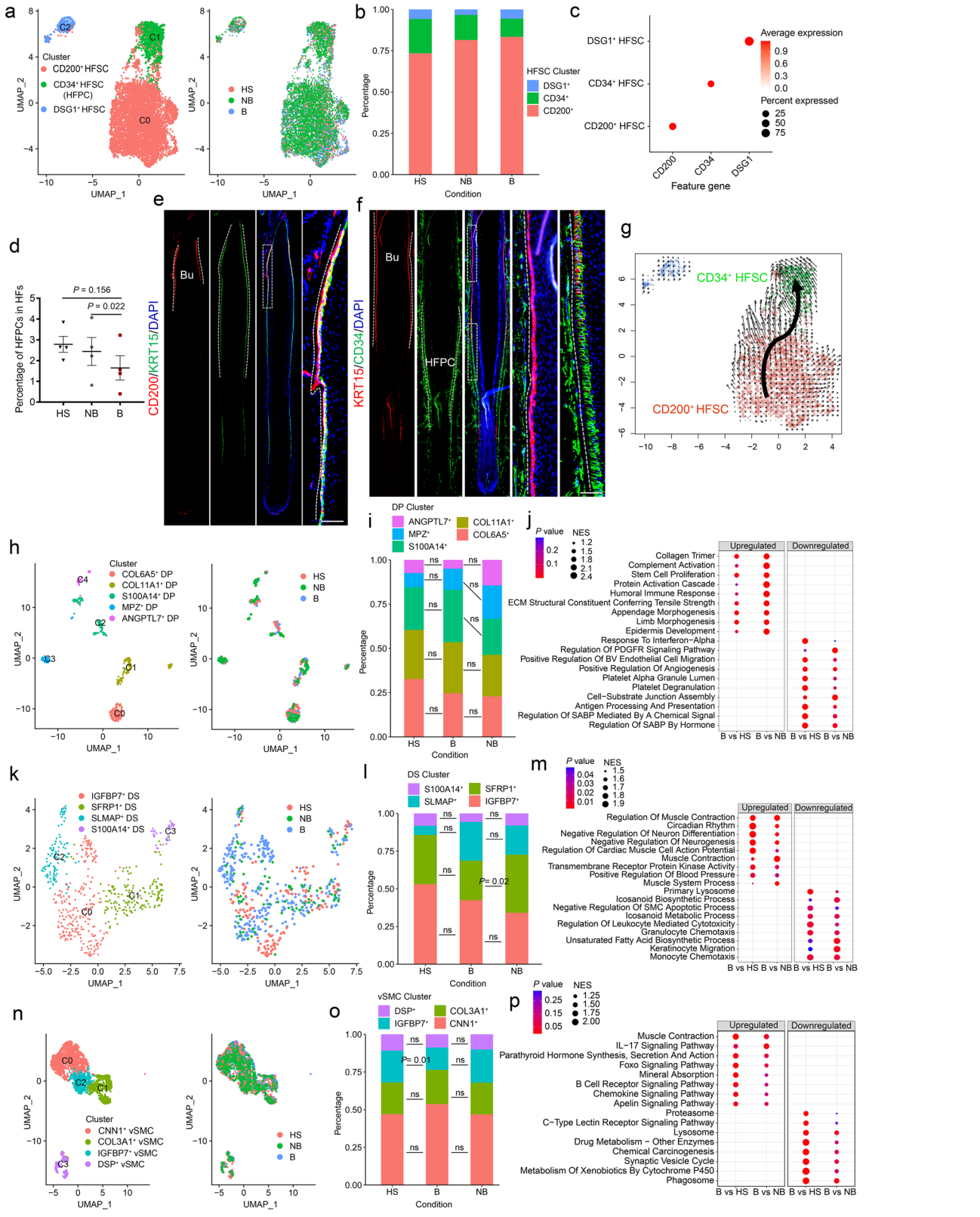

versus other subpopulations. Top marker genes with avg_log2FC > 0.25, pct (minimum fraction in either of the two populations)>0.25 and *P* value < 0.05 of each subcluster were showed in Supplementary Data 7. Among these, KRT15 was commonly highly expressed (Fig. S2f); CD200 was visibly enriched in subcluster 0 (CD200$^+$ HFSCs), while CD34 was mainly enriched in subcluster 1 (CD34$^+$ HFSCs), and subcluster 2 was enriched with DSG1 (DSG1$^+$ HFSCs) (Fig. 2c). Consistently, CD34$^+$ HFSCs were decreased in balding anagen HFs (Fig. 2d). By immunostaining, we defined that CD200$^+$ HFSCs are located in the upper bulge with high stemness, while CD34 is mainly expressed in the lower bulge cells referred to as HF progenitor cells (HFPCs), which are differentiated from the upper bulge HFSCs (Fig. 2e, f). Via RNA Velocyto analysis, we further confirmed that CD200$^+$ HFSCs have the ability to differentiate into CD34$^+$ HFSCs (namely HFPCs) (Fig. 2g). As progeny

Fig. 2 | Heterogeneity of cell subpopulations in AGA and healthy scalps. a UMAP plots showing subclusters and sample conditions of HFSCs. **b** Bar graph representing the percentage of subpopulations of HFSCs. **c** Dot plot showing the expression of CD200, CD34 and DSG1 in each HFSC subcluster via scRNA-seq. **d** The percentage of $CD34^+$ HFSCs (HFPCs, hair follicle progenitor cells) in HS, NB and B HFs. HFs were obtained from 4 healthy individuals and from non-balding and balding scalp regions of 4 androgenetic alopecia patients. Representative immunostaining images showing CD200 expression in upper bulge stem cells (**e**) and CD34 expression in progenitor cells (**f**), with magnified views of boxed regions. Nuclei are counterstained with DAPI (blue). Dashed lines indicate the outer root sheath–dermal sheath boundary. Bu, bulge, Scale bar, 50 μm. **g** RNA velocity analysis showing inferred differentiation trajectories of hair follicle stem cell subclusters. **h** UMAP plots showing subclusters and sample conditions of DP cells. **i** Bar graph representing the percentage of subpopulations of DP cells. **j** Representative Gene Ontology (GO) terms of upregulated (left) and downregulated (right) DEGs between balding and healthy groups (B vs. HS), balding and non-balding groups (B vs. NB) in DP cells. NES stands for enrichment scores. The color keys from red to blue indicate the range of *P* value. UMAP plots **(k)** and relative proportions (**l**) of dermal sheath cell subclusters. **m** Representative Gene Ontology terms enriched in dermal sheath cells from balding versus non-balding or healthy scalp regions. UMAP plots **(n)** and relative proportions **(o)** of vascular smooth muscle cell subclusters. **p** Representative GO terms enriched in vSMC from balding versus non-balding or healthy scalp. Data are presented as mean ± SEM. Statistical significance was assessed using two-tailed paired Student's *t* tests for comparisons between balding and non-balding scalp regions and two-tailed unpaired Student's *t* tests for comparisons between balding and healthy scalp regions. *P* values are indicated; ns, not significant.

of HFPCs, matrix cells were also found to be decreased in the balding HFs of AGA patients (Fig. S5a).

Subclustering of DP cells, the signaling center for hair growth[28], revealed 5 subclusters (Fig. 2h; Fig. S5b and Supplementary Data 8). The percentage and distribution of subclusters were comparable across HS, NB and B, suggesting that DP cell identity may not alter in AGA anagen HFs (Fig. 2i and Supplementary Data 9). Gene ontology (GO) analysis showed that pathways involving collagen trimer, appendage morphogenesis and epidermis development were upregulated in B DP cells (Fig. 2j); while angiogenesis-related pathway was downregulated (Fig. 2j), consistent with our previous findings from bulk RNA sequencing[19].

DS cells were divided into 4 subclusters (Fig. 2k; Fig. S5c and Supplementary Data 10), which showed no significant changes in the balding anagen HFs of AGA patients (Fig. 2l and Supplementary Data 11). Pathway enrichment analysis of differential genes revealed muscle contraction was obviously upregulated in balding anagen HFs compared to non-balding or healthy groups (Fig. 2m).

In human hair follicle, the DS is tightly surrounded by a network of blood vessels, composed of vSMCs and endothelial cells[57]. Among them, vSMCs were separated into 4 subclusters, and the percentage and distribution of subclusters were comparable across three groups (Fig. 2n, o; Fig. S5d; Supplementary Data 12 and 13). Pathway enrichment analysis showed that smooth muscle contraction and multiple pathways involved in inflammatory regulation (such as IL-17 signaling pathway) were upregulated in vSMCs of balding anagen HFs (Fig. 2p). Endothelial cells were divided into 4 subclusters, which exhibited no obvious alterations (Fig. S5e–g; Supplementary Data 14 and 15), and IL-17 signaling pathway was also upregulated in endothelial cells of balding anagen HFs (Fig. S5h).

Immune cells expressing CD3D were further separated into 6 subclusters, including Th17 cells ($IL17A^+$/$IL17F^+$), naive $CD4^+$ T cells ($IL7R^+$), $CD8^+$ T cells ($GZMK^+$/$CD8A^+$), natural killer T (NKT) cells ($ZNF683^+$) and two unknown subclusters (Fig. S5i–k and Supplementary Data 16). Cell composition analysis and co-immunostaining of CD4 and IL17A showed significant increase of Th17 cells in balding HF units (Fig. S5l–n; Supplementary Data 17), which provides evidence for inflammatory infiltration in AGA.

Identification of early changes in HFSC fate determination and cell–cell communications in AGA

Epidermal and sebaceous differentiation of HFSCs has been reported to be associated with HF miniaturization during ageing-induced and obesity-induced hair loss in mice[58,59], but it was unclear whether there existed HFSC fate determination alterations in AGA development. To address this question, we conducted cell fate analysis among potential cell types: HFSCs, HF lineage (including ORS basal and matrix cells), IFE lineage (including Outer II and IFE basal cells) or sebaceous gland cells. As expected, more HFSCs showed a pronounced tendency to differentiate into IFE lineage and sebaceous gland cells in balding HFs compared with non-balding and healthy HFs, and obviously, decreased HFSCs differentiated into HF lineage cells (Fig. S6a, d). To explore the underlying mechanisms, branched expression analysis modeling (BAEM) was performed, and identified three common cell fate determination genes, COL17A1, PPP1R1C, and SGK1 (Fig. S6b, c, e, f).

To further characterize the cell–cell communications between different cell types in HF units. Cellchat[40] was employed to compare the cell–cell communications between balding and non-balding/healthy HFs. Although the interaction strength showed that most cell types had no obvious changes in incoming and outgoing interaction strength, Th17 cells, SwGs, and SGDCs exhibited increased incoming interaction strength in balding and non-balding HFs compared to healthy HFs, while HFSCs and outer II cells displayed decreased outgoing interaction strength in balding anagen HFs in AGA (Fig. S6g).

Apoptotic loss of HF progenitor cells is correlated with HF miniaturization in AGA

AGA is characterized by the progressive conversion of the terminal (t) scalp HFs into intermediate/miniaturized (i/m) HFs, which we called the process of HF miniaturization and may be attributed to the deficiency of HFSCs and their descendant cells (such as progenitor cells and matrix cells) based on our results as mentioned above (Fig. 2b, d; Fig. S5a) and the early study[33]. To verify changes in HFSC and progenitor cell numbers, we performed immunostaining of CD200 and CD34 on anagen HFs from frontal balding (B) and occipital non-balding scalps (NB) of AGA patients, and frontal normal scalps of healthy individuals (HS). HFs retain $CD200^+$ HFSCs with the same percentage in AGA, despite a decrease in cell numbers in B scalps (Fig. S7a–c). However, $CD34^+$ progenitor cells were gradually diminished during the process of HF miniaturization (Fig. 3a–c). Further analysis indicated a strong positive correlation between the number/proportion of $CD34^+$ progenitor cells and the hair follicle diameter in balding scalps of AGA patients (Fig. 3d–g). Collectively, these observations suggest that loss of progenitor cells is associated with HF miniaturization in AGA.

Next, an investigation into the causes of the progenitor cell loss via signaling pathway enrichment analysis revealed upregulated apoptotic signals in progenitor cells of balding anagen HFs (Fig. 3h). A significant increase in apoptosis was observed in the $CD34^+$ progenitor cells of balding anagen HFs according to Cleaved Caspase-3 staining (Fig. 3i, j). These results support the notion that an apoptosis-induced gradual loss of $CD34^+$ progenitor cells may be involved in the development of AGA.

Hyperactive CTS contraction suppresses hair follicle growth via inducing progenitor cell apoptosis and inhibiting ORS and matrix cell proliferation in AGA

Intimate crosstalk between stem cells and the surrounding microenvironment is vital for stem cell fate decisions. On the outside of the progenitor cells is the structure of DS (mainly composed of a layer of elastic DS cells) in murine pelage HF, while in human scalp HF is the

https://doi.org/10.1038/s41467-026-70153-4

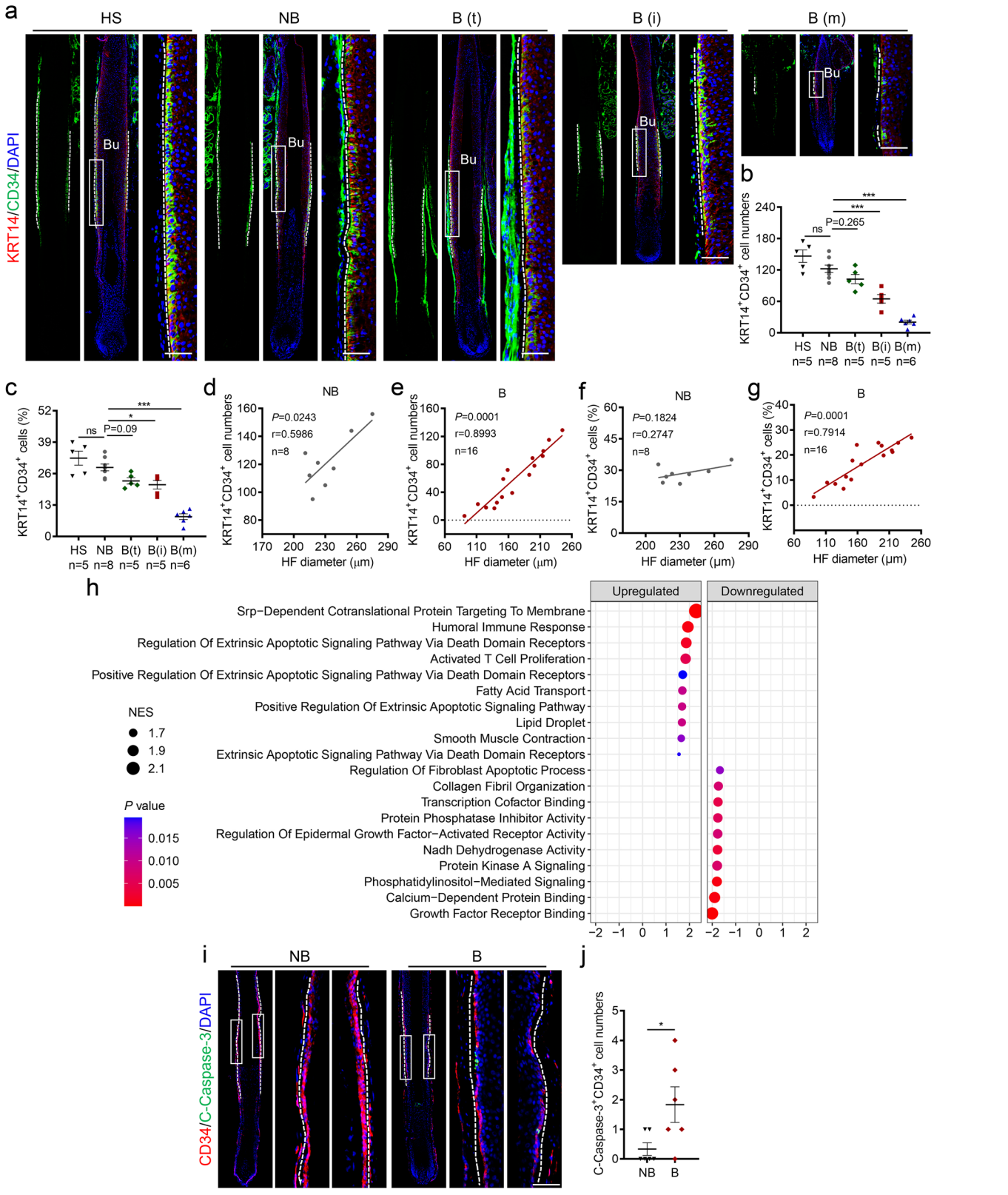

multi-layer of connective tissue sheath (CTS, the homolog of murine DS) mainly composed of DS cells, collagens and vasculature (including vSMCs and endothelial cells)[57](Figs. 4a, b and S8a). Pathway enrichment analysis revealed increased contractile activity in both DS cells and vSMCs of balding anagen HFs compared to non-balding or healthy groups (Fig. 2m, p), which can be supported by the immunostaining of phosphorylated myosin light chain 2 (p-MLC2), a marker of myosin active state[60] (Figs. 4c, d and S8b, c). To further confirm whether DS cells in balding anagen HFs exhibit enhanced contractility or acquire hypercontractility under specific stimuli, we first profiled the expression of mechanocontractile receptors. CHRM3 and EDNRA emerged as the two most abundantly expressed receptors in DS cells (Fig. S8d). Subsequent co-immunostaining analysis confirmed that CHRM3 is specifically expressed within the CTS compartments (encompassing

Fig. 3 | Apoptotic loss of HF progenitor cells is associated with HF miniaturization in AGA. a Representative immunostaining images showing progenitor cells in anagen hair follicles from healthy scalps ($n = 5$ HFs), non-balding scalp regions ($n = 8$ HFs), and balding scalp regions classified as terminal ($n = 5$), intermediate ($n = 5$), or miniaturized ($n = 6$) HFs, obtained from 3 AGA patients. Epidermal cells and progenitor cells are labeled with KRT14 (red) and CD34 (green), respectively. Dashed lines indicate the outer root sheath–dermal sheath boundary. Scale bar, 50 μm. Types of HFs were defined by their diameter. Terminal (t): diameter>200 μm; Intermediate (i): 150 μm <diameter<200 μm; mini (m): diameter<150 μm. Quantification of the number of $KRT14^+CD34^+$ progenitor cells in different groups (**b**) and their proportion (**c**) in the total outer layer of HFs (n for HS/NB/B(t)/B(i)/B(m) = 5/8/5/5/6 anagen HFs). **d**–**g** Correlation analyses between hair follicle diameter and progenitor cell number or proportion in androgenetic alopecia patients. Spearman's correlation coefficient (two-tailed) was used. **h** Top 10 GO terms upregulated or downregulated in progenitor cells (B vs. NB). Representative images (**i**) and quantification (**j**) of cleaved Caspase-3-positive and CD34-positive progenitor cells in anagen HFs from NB and B scalps of AGA patients ($n = 6$ HFs from 3 donors for each group); Right panels, magnified images of boxed areas Progenitor cells were indicated with dotted line. Scale bar, 50 μm. Data are presented as mean ± SEM. Statistical significance was assessed using one-way analysis of variance with Tukey's post hoc test (**b**, **c**) or two-tailed unpaired Student's t tests (**j**). P values are indicated in the Source data file. $^*P < 0.05$, $^{**}P < 0.01$, $^{***}P < 0.001$, ns, not significant.

DS cells and vSMCs), with comparable expression levels in NB and B anagen HFs (Fig. S8e). Although EDNRA was detectable in human HFs, its expression localized primarily to the ORS cells with minimal CTS presence (Fig. S8f). Notably, serum concentrations of acetylcholine (ACH)—a canonical agonist of CHRM3—were significantly elevated in AGA patients compared to healthy controls. Moreover, ACH levels were higher within B HFs relative to NB HFs (Fig. S8g). We also observed that stimulation with methacholine (MCH, a synthetic ACH derivative[61–63]) induced greater Young's modulus and more pronounced contractility in isolated primary DS cells derived from B HFs of AGA patients versus NB controls (Fig. S8h-k). Crucially, at the organ-culture level, MCH stimulation provoked significantly stronger contraction in B HFs compared to NB HFs, recapitulating the cellular phenotype (Fig. 4e, f). Collectively, these results suggest that CTS contraction is enhanced in anagen HFs of balding scalps in AGA patients.

Given that the contractile force of DS is a key driver of HF regression in mice[29], we wondered whether excessive contraction of the CTS, the analogous structure of murine DS in human, might affect hair follicle growth in AGA. To this end, we utilized MCH to activate CTS contraction in the in vitro cultured human anagen HF organs. The efficiency of MCH on CTS contraction in this model was evaluated and verified by p-MLC2 immunostaining and real-time confocal imaging (Fig. S9a–c). Strikingly, MCH treatment resulted in a dose-dependent negative effect on hair growth and anagen maintenance (Figs. 4g–i and S9d). Given the marked depletion of progenitor cells in AGA-affected balding HFs, we sought to investigate whether hyperactive CTS contraction could potentially mediate pathological effects on these progenitor populations. Our results showed that MCH promoted the loss and apoptosis of $CD34^+$ progenitor cells in a concentration-dependent manner. Of note, Cleaved Caspase-3^+CD34^+ cells are barely detectable under 100 μM MCH treatment due to the fact that $CD34^+$ progenitor cells were almost depleted under this condition (Fig. 4j–m). Given the crucial role of epidermal cell proliferation—particularly matrix cells—in HF growth, we examined the proliferative activity of the HF compartments, and found that MCH suppressed proliferation in both matrix and ORS cells in a dose-dependent manner (Fig. 4n, o). Notably, blockade of CTS contraction with ML-7 (Fig. S9b, c, e), a specific myosin activation inhibitor[64], not only improved the growth retardation and catagen premature induction (Figs. 4p-r and S9f), but also reversed the apoptotic loss of progenitor cells and the inhibited proliferation of matrix and ORS cells in MCH-treated human HFs (Fig. 4s-x), confirming the critical role of CTS contraction in MCH effects.

Prompted by a recent study demonstrating dihydrotestosterone (DHT, converted from testosterone via 5α-reductase) promotes muscle cell contraction via the membrane receptor GPR133[65], we wondered whether DHT might similarly stimulate CTS contraction through GPR133 in AGA pathogenesis. We first examined GPR133 expression and found that it is indeed expressed in human HF CTS cells (Fig. S10a). Via immunoblotting, we showed that primary DS cells treated with DHT exhibited significantly upregulated MLC2 phosphorylation levels (Fig. S10b, c), while atomic force microscopy (AFM) confirmed enhanced cellular contractility (Fig. S10d); these DHT-induced effects were reversed by ML-7 treatment (Fig. S10c, d). Moreover, real-time confocal imaging directly validated DHT-induced contraction enhancement in both DS cells and intact human hair follicles (Fig. S10e–h). Further HF organ culture experiments showed that DHT not only induced CTS hypercontraction, but also triggered progenitor cell apoptosis, suppressed matrix and ORS cell proliferation, and ultimately inhibited HF growth—all of which were significantly reversed by either GPR133 knockdown (Fig. S10i–r) or ML-7 treatment (Fig. S11a–i). To be mentioned, while AR knockdown alleviated DHT's inhibitory effects on HF growth, it did not alter CTS contraction (Fig. S11j–m). Consistently, we observed markedly reduced proliferative activity in matrix and ORS cells within balding HFs of AGA patients, accompanied by a significant increase in the proportion of HFs in the catagen phase (Figs. 4y, z and S12a–c). These findings significantly strengthen the link between enhanced CTS contraction and AGA pathogenesis.

Subsequently, to determine whether apoptosis is necessary, we applied Z-VAD-FMK to block cell apoptosis[66]. Our results showed that the observed phenotypes caused by MCH, including HF growth inhibition (Fig. S13a–c), premature catagen induction (Fig. S13d) and depletion of $CD34^+$ progenitor cells (Fig. S13e–h), were partially improved after Z-VAD-FMK administration.

Taken together, these data suggest that over-activated CTS contraction compresses HF growth via induction of progenitor cell apoptosis and suppression of matrix and ORS cell proliferation.

CTS contraction induces progenitor cell apoptosis and inhibits ORS and matrix cell proliferation via PIEZO1 signaling

To pinpoint the specific molecular mechanisms by which the contractility of CTS mediates this effect, we first examined the expression levels of the known mechanosensitive ion channel proteins, which have been found to be expressed in HFs in mice[67]. Our results showed that of the eight mechanosensitive ion channel genes investigated, *PIEZO1* was abundantly expressed across HFSCs (including progenitor cells), ORS and matrix cells (Fig. 5a, b) and was expressed at higher levels in balding anagen HFs compared to non-balding group (Fig. S14a, b). We then used intracellular Ca^{2+} as a downstream indicator of PIEZO1 signaling[68,69]. As quantified by Cal520 (a Calcium influx indicator[70]) relative fluorescent intensity (RFI), there was a significant increase in intracellular Ca^{2+} concentration in ORS (including progenitor cells) and matrix cells of balding anagen HFs (Fig. 5c, d). These results suggest that PIEZO1 signaling is activated in ORS and matrix cells of balding anagen HFs.

We next investigated whether activation of PIEZO1 is sufficient to induce HF growth retardation. To this end, we applied YODA1, a PIEZO1-specific activator to cultured anagen HFs (Fig. S14c, d). Intriguingly, anagen HFs treated with YODA1 displayed a phenotype similar to MCH, including growth retardation, progenitor cell apoptosis, and inhibited proliferation of ORS and matrix cells (Fig. 5e–m and Fig. S14e). In addition, the Ca^{2+} concentration in MCH-treated HF ORS

https://doi.org/10.1038/s41467-026-70153-4

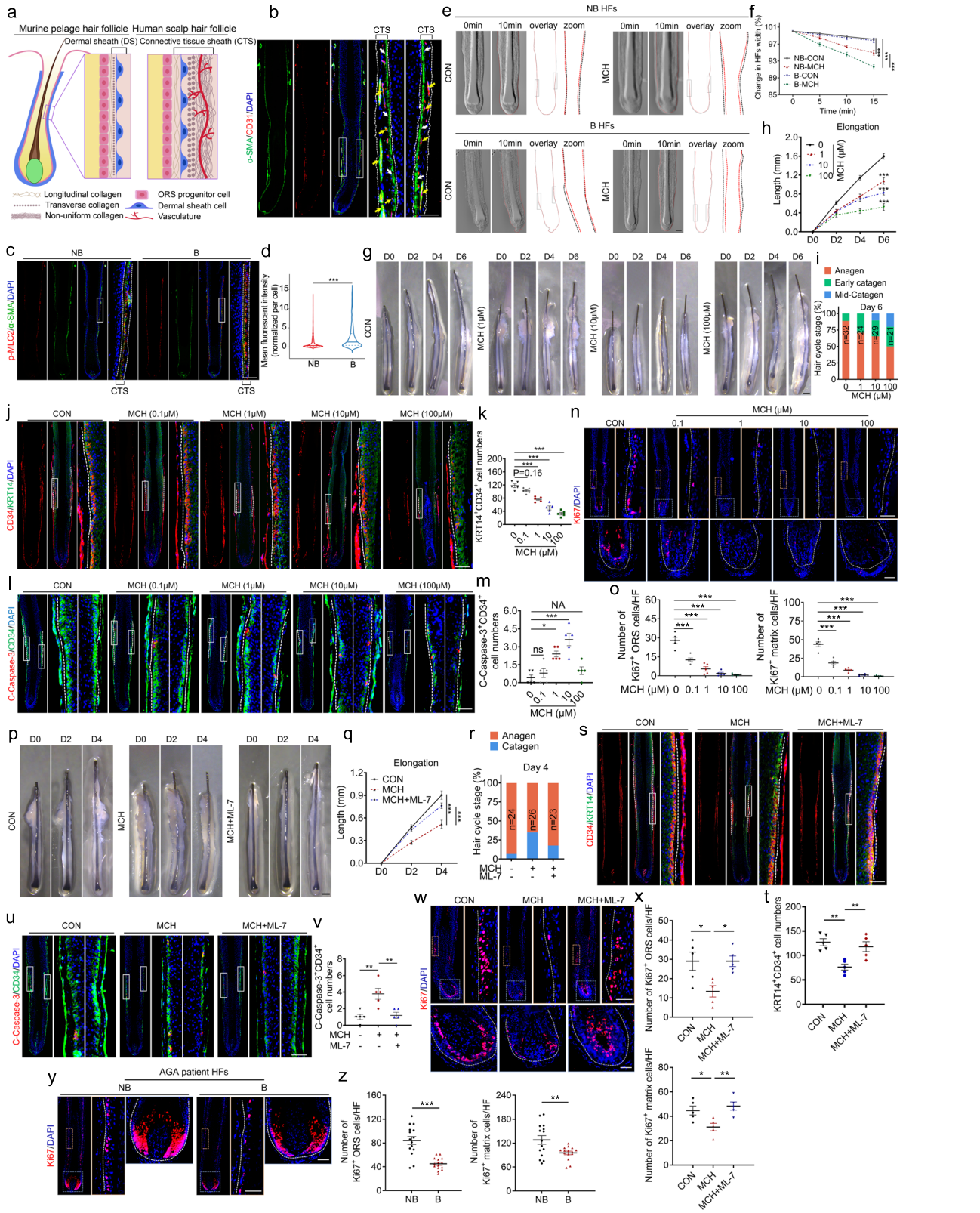

and matrix cells was elevated and could be reversed by the specific PIEZO1 inhibitor GsMTX4 and the myosin activation inhibitor ML-7 (Fig. S14f, g), indicating the activation of PIEZO1 signaling by CTS contraction. Not surprisingly, inhibition of PIEZO1 signaling by GsMTX4 rescued the phenotypes induced by MCH (Fig. 5n–v and Fig. S14h). To further ascertain whether PIEZO1 activation directly suppresses proliferation and induces apoptosis in matrix and ORS cells, we treated primary human ORS cells in vitro with YODA1. Our results demonstrated that activation of PIEZO1 by YODA1 not only significantly suppressed ORS cell proliferation but also potently induced apoptosis (Fig. S14i, j). Furthermore, PIEZO1 activation directly elevated intracellular calcium, compromised mitochondrial function, and upregulated the apoptotic executioner molecule cleaved caspase-3 in ORS cells (Fig. S14k–m). Given that *TRPV4* was also

Fig. 4 | Hyperactive CTS contraction suppresses hair follicle growth in AGA. **a** Dermal sheath (DS)/ connective tissue sheath (CTS) in murine pelage follicle/ human scalp follicle. This image is adapted from the previous publication[57]. **b** Immunostaining of CD31 (Endo marker) and α-smooth muscle actin (marker of DS and vSMCs) in anagen human scalp HFs. Dashed lines indicate the CTS. **c** Immunostaining of phosphorylated myosin light chain 2 (p-MLC2) in anagen HFs from NB and B scalp regions of AGA patients. Right panels, magnified images of boxed areas. **d** Quantification of relative fluorescence intensity of p-MLC2 in α-smooth muscle actin–positive CTS cells ($n = 959$ DS cells from 5 NB HFs and 1838 DS cells from 10 B HFs, from 3 AGA patients). **e** Representative real-time confocal images of anagen HFs treated with melanocyte-concentrating hormone (MCH), showing morphological changes at 0 and 10 min. **f** Quantification of changes in HF width over time ($n = 6$ HFs from 3 AGA patients per group). Representative images **(g)** and quantification **(h)** of hair shaft elongation in ex vivo–cultured anagen HFs treated with MCH at the indicated concentrations ($n = 21$–32 HFs from 3 donors per group). **i** Quantification of HF cycle stage on day 6. **j**–**o** Immunostaining and quantification of HFPC number (CD34 and KRT14), apoptosis (cleaved caspase-3), and proliferation (Ki67) in ex vivo–cultured HFs ($n = 5$ HFs from 3 donors per group). **p**–**x** Rescue experiments showing the effects of myosin light chain kinase (MLCK) inhibition on hair shaft elongation, HFPC survival, and epithelial proliferation ($n = 23$–26 HFs from 3 donors per group for hair elongation quantification and $n = 5$ HFs from 3 donors per group for staining). Immunostaining **(y)** and quantification **(z)** of Ki67$^+$ ORS or matrix cell numbers per HF in NB and B anagen HFs from AGA patients ($n = 15/15$ HFs from 5 AGA patients). Scale bar, 50 μm (**b**, **c**, **j**, **l**, **n**, **s**, **u**, **w**, **y**), 100 μm (**e**), 200 μm (**g**, **p**). Data are expressed as mean ± SEM and were analyzed by one-way ANOVA with Tukey's post hoc test (**k**, **m**, **o**, **t**, **v**, **x**) and two-way ANOVA with a post hoc Holm–Sidak's multiple comparisons test (**f**, **h**, **q**), or two-side unpaired Student's *t* test (**d**, **z**). *P* values are indicated in Source data file. $^*P < 0.05$, $^{**}P < 0.01$, $^{***}P < 0.001$. ns, not significant. NA, not applicable.

abundantly expressed in HFSCs and ORS cells (Fig. 5a), we sought to investigate whether it also mediates CTS hypercontraction-induced hair growth retardation. Consequently, treating MCH-challenged human anagen HFs with the selective TRPV4 inhibitor RN17347[71], demonstrated that TRPV4 blockade failed to rescue the MCH-mediated suppression of HF growth (Fig. S14n, o).

Targeting CTS contraction by ML-7 improves the growth of HFs from the balding scalps of AGA patients

All the above results inspired us to wonder whether targeting CTS contraction is a promising therapy for AGA. We first obtained anagen HFs from the balding scalps of AGA patients, which had been experiencing the process of miniaturization. As expected, the balding anagen HFs exhibited slower growth compared with those from occipital non-balding scalps of the same AGA patients in ex vivo organ culture system (Fig. S15a–c). We then treated the balding HFs with ML-7, or minoxidil (MNX), the FDA-approved drug for AGA treatment. Immunostaining of p-MLC2 confirmed that ML-7 abolished muscle contraction activity in CTS, but MNX did not (Fig. S15d). Excitingly, ML-7 could significantly improve the growth and premature regression of balding HFs of AGA patients, even better than MNX (Fig. S15e–h). Consistently, ML-7 showed a better effect on decreasing the apoptotic loss of progenitor cells compared with MNX (Fig. S15i, j). Furthermore, we demonstrated ML-7 did not affect the growth and anagen-to-catagen progression of cultured anagen HFs from occipital non-balding scalps of AGA patients, suggesting a specific therapeutic effect for balding anagen HFs with enhanced CTS contraction (Fig. S15k–m).

Given the recent development of an excellent humanized mouse model for preclinical AGA research[26,72,73], we wondered whether targeting CTS contraction via ML-7 demonstrates therapeutic efficacy in this system. We first established the humanized mouse model by transplanting human scalps from non-balding and balding regions of AGA patients on SCID mice according to previous studies[26,72]. Using this humanized mouse model, we demonstrated that administration of MCH enhanced CTS contraction, induced apoptosis in the ORS cells (including progenitor cells), suppressed the proliferation of matrix and ORS cells, and inhibited HF growth; conversely, application of ML-7 effectively countered these effects, markedly improving the phenotypes induced by MCH within xenografted hair follicles derived from the non-balding scalps of AGA patients (Fig. 6a–f, and Fig. S16a–d). Similarly, in this humanized mouse model, DHT treatment phenocopied MCH-induced pathological manifestations within xenografted non-balding HFs of AGA patients, while ML-7 markedly ameliorated these DHT-triggered phenotypes—manifesting as HF growth retardation, progenitor cell apoptosis, and suppressed proliferation in both ORS and matrix cells (Fig. 6g–l, and Fig. S16e–i). We further compared the therapeutic efficacy of ML-7 versus minoxidil and their combination in this humanized mouse models. Our results showed that both ML-7 and MNX significantly rescued DHT-induced hair growth suppression, while their combination demonstrated superior therapeutic outcomes (Fig. 6m–r). However, no statistically significant difference was observed between ML-7 and MNX monotherapies in vivo (Fig. 6m–r), contrasting with our prior ex vivo human HF organ culture data where ML-7 outperformed MNX (Fig. S15e–j). Most importantly, our longitudinal observations revealed that ML-7, administered for over one month, prominently improved hair growth even within xenografted HFs derived from the balding scalps of AGA patients (Fig. 6s–x).

Taken together, we propose that hyperactive CTS contraction in balding anagen HFs activates PIEZO1 signaling in ORS and matrix cells via mechano-transduction, thereby inducing cell apoptosis and suppressing cell proliferation, ultimately resulting in HF growth retardation (Fig. S17), which strongly suggests that relaxing HFs via targeting CTS contraction is a hopeful strategy for AGA therapy.

Discussion

Here, we present a comprehensive single-cell transcriptomic and spatial analysis of human hair follicle (HF) units from balding and non-balding scalp regions of androgenetic alopecia (AGA) patients, alongside healthy individuals. Considering that HFs of balding scalps used in the present study were in anagen phase and at the early stage of pathogenesis, isolated from the edge of the frontal hairline of AGA patients, our high-quality data allowed us to illustrate the early changes in cell subpopulations, the HF cell lineage trajectory and cell–cell communications in AGA in unprecedented detail. Our atlas uncovers at least 20 different broad cell types in the human HF unit, which are more than those described in previous scRNA-seq studies[45,46]. The reason for this obvious difference could be likely attributed to the optimization of human HF single cell isolation by combining mechanical separation with multienzyme digestion. Based on this, we obtained previously undescribed DP cells and major cell types of CTS (including DS, vSMC and endothelial cells) in human HFs, which are reported to be essential for regulating the growth of hair follicles[29,57,74]. Delineation of DP and CTS cells at single-cell level provides an opportunity to determine the precise roles of these cells in the pathogenesis of AGA.

The hair growth is powered by HFSCs (termed as bulge stem cells) that have the ability to give rise to all epithelial components of the hair follicle[75]. Human HFSCs contain two major subclusters: CD200$^+$ stem cells and CD34$^+$ progenitor cells[34]. Previous study has revealed that balding scalp in men with AGA retains CD200$^+$ HFSCs but lacks progenitor cells[33]. However, the mechanistic insights underlying the loss of HF progenitor cells are not entirely elucidated. Here, we confirm the findings regarding the loss of progenitor cells in AGA. Importantly, we demonstrate that aberrant CTS contraction drives this loss via apoptosis induction and concurrently suppresses the proliferation of matrix and ORS cells, potentially representing a key driver underlying HF miniaturization in AGA. Besides, we demonstrate that HFSCs are

https://doi.org/10.1038/s41467-026-70153-4

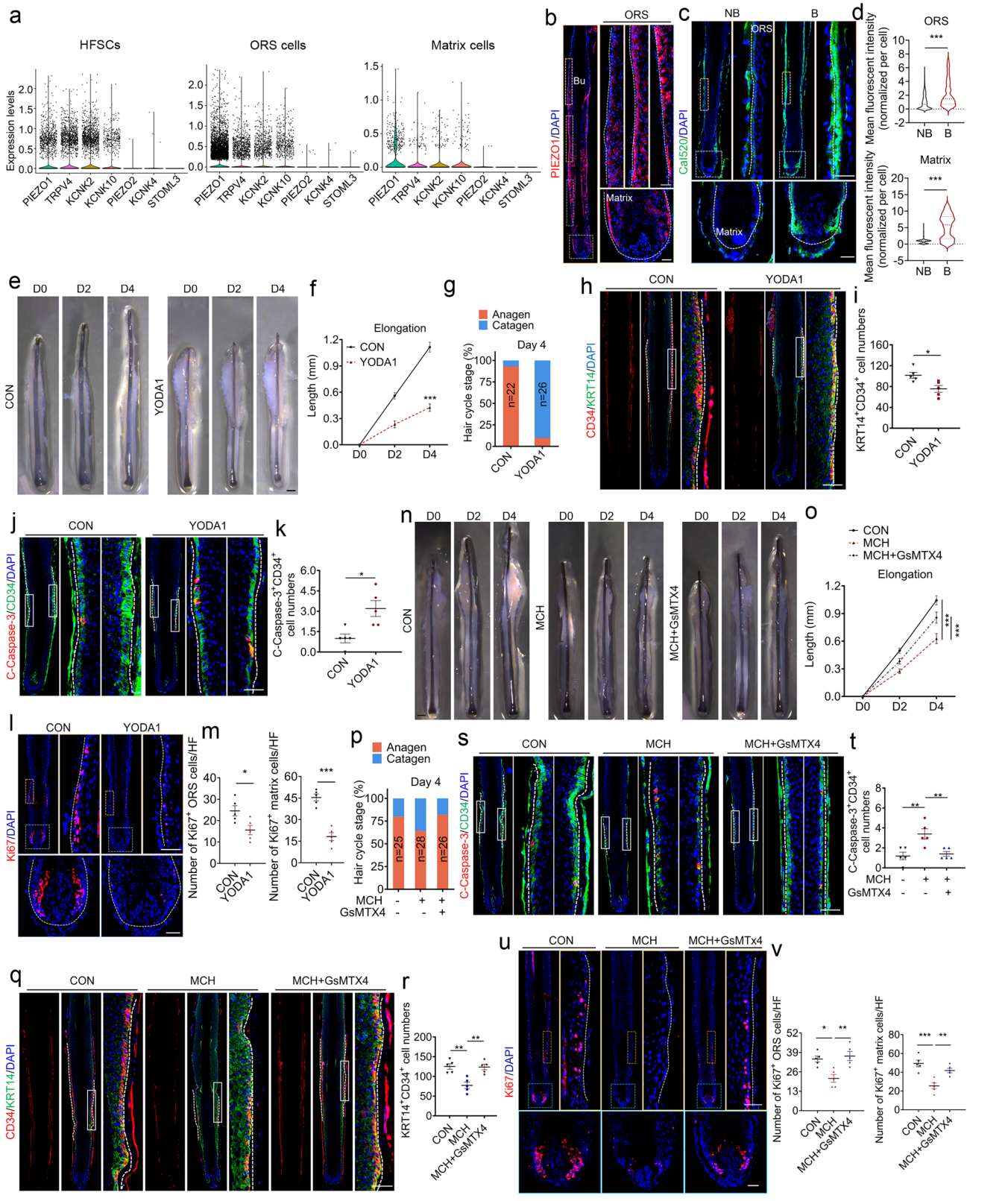

more likely to differentiate into interfollicular epidermal and sebaceous lineages, rather than HF lineage cells, in the balding scalps, which may be responsible for the progressive hair follicle miniaturization and hair thinning in AGA. Similarly, in the case of ageing- and obesity-induced hair loss in mice, those aberrant fate changes also occur in a fraction of HFSCs, which prefer to undergo epidermal and sebocyte differentiation regulated by COL17A1 proteolysis and inflammatory signals, respectively, thereby decreasing the HFSC pool and leading to hair follicle miniaturization in a stepwise manner[58,59]. Here, our data also suggest an important role of COL17A1 in the aberrant differentiation of HFSCs in AGA development. During normal hair growth, HF stem/progenitor cells proliferate and differentiate to generate hair matrix cells, which rapidly proliferate to produce the hair shaft of growing hair in the end[76]. Consistent with impaired progenitor output,

Fig. 5 | PIEZO1 signaling is necessary for CTS contraction-induced HF growth retardation. a Violin plots showing expression of mechanosensitive ion channels in HFSCs, ORS cells, and matrix cells identified by scRNA-seq. TRPA1 expression was undetectable. **b** Representative immunostaining of PIEZO1 on HFs from NB occipital scalps of AGA patients. Calcium imaging using Cal520 in anagen HFs from NB and B scalp regions (**c**), and quantification of mean fluorescence intensity in ORS (including HFPCs) and matrix cells (**d**; $n = 1{,}002/810$ ORS cells and 328/287 matrix cells from 6 NB and 6 B HFs from 3 AGA patients). ORS–DS boundary is indicated by dashed lines. Representative images (**e**) and quantification (**f, g**) of hair shaft elongation and HF cycle stage in ex vivo–cultured HFs treated with the PIEZO1 agonist YODA1 ($n = 22$–26 HFs from 3 donors per group). **h**, **m** Immunostaining and quantification of HFPC number, apoptosis, and proliferation following PIEZO1 activation ($n = 5$ HFs from 3 donors per group). **n**–**v** Effects of PIEZO1 inhibition on HF growth, HFPC survival, and epithelial proliferation in ex vivo HFs treated with MCH ($n = 25$–28 HFs from 3 donors per group; r,t,v, $n = 5$ HFs per group). Right panels, magnified images of boxed areas. Scale bar, 50 μm (**b**, **c**, **h**, **j**, **l**, **s**, **q**, **u**), 200 μm (**e**, **n**). Data are expressed as mean ± SEM and were analyzed by one-way ANOVA with Tukey's post hoc test (**r**, **t**, **v**), two-way ANOVA with a post hoc Holm–Sidak's multiple comparisons test (**f**, **o**), and two-tailed unpaired Student's *t* test (**d**, **i**, **k**, **m**). *P* values are indicated in Source data file. $^{*}P < 0.05$, $^{**}P < 0.01$, $^{***}P < 0.001$.

proliferative matrix cells are also reduced in balding hair follicles, providing a cellular basis for diminished hair shaft production.

Hair follicle miniaturization is widely understood within a DP-centric framework, defined by progressive reductions in DP volume, cell number, and inductive capacity, followed by impaired generation of epithelial progeny from bulge stem cells[4,5,28,77]. Our previous study demonstrated that androgen receptor (AR) is upregulated in DP cells, which induce apoptosis of microvascular endothelial cells via paracrine signaling in the DP of balding HFs in AGA[19]. However, in this study, except for the downregulated angiogenesis, our scRNA-seq analysis identifies no other obvious changes in cell subpopulations and signaling pathways, which may be involved in the regulation of hair growth, in DP cells of balding HFs from AGA patients. The reasons for this discrepancy are currently not clear, and further analysis and experimentation will be required to address this point. Although microinflammation has been commonly reported in AGA[78–81], the details remain largely undefined. Here, we identity that T cells are the main lymphocytes in human HF units, and AGA is featured by increased Th17 cells, suggesting a potential contribution of adaptive immune responses to follicular pathology.

HF growth is tightly spatiotemporally regulated by the crosstalk between stem/progenitor cells and the microenvironment, mainly the mesenchymal niche[27]. In addition to the well-established role of the dermal papilla (DP), the dermal sheath (DS)—which is continuous with the DP and envelops the HF—represents an important but comparatively understudied niche component[57]. While the DS has been shown to function as a smooth muscle driving follicle regression during catagen in mice[29,82], the role of its human counterpart, the connective tissue sheath (CTS), particularly under pathological conditions, has remained unclear. Focusing on anagen follicles from balding scalp regions of androgenetic alopecia patients, we demonstrate that smooth muscle contraction–associated programs are aberrantly upregulated in CTS components, including DS cells and vascular smooth muscle cells, and that pathological CTS hypercontractility impairs HF growth by inducing progenitor cell apoptosis and suppressing outer root sheath and matrix cell proliferation. Pharmacological inhibition of CTS contraction via ML-7 exhibits hair growth–promoting effects comparable to those of minoxidil, the only FDA-approved topical agent for AGA, and combined treatment produces a greater stimulatory effect than either agent alone, suggesting a complementary mechanism of action. Of note, as finasteride, the most commonly prescribed oral therapy for AGA, acts upstream by inhibiting DHT production, its efficacy cannot be meaningfully evaluated or directly compared with CTS-targeting strategies within the current model systems. Future clinical studies will be required to determine the exact therapeutic efficacy of targeting CTS contraction and to evaluate its potential for combination treatment with existing therapies in AGA patients.

We further identify PIEZO1 as a key mediator of CTS-induced epithelial dysfunction. PIEZO1 was prioritized based on its relatively higher expression, consistent activation signatures, and functional responsiveness in our experimental systems. Although other mechano-transducers are expressed in hair follicle compartments, their potential contributions were beyond the scope of the present study. Hyperactivation of PIEZO1 triggers apoptosis in HF progenitor cells, suppresses proliferation in ORS (containing progenitor cells) and matrix cells, and consequently inhibits human hair growth; conversely, inhibition of PIEZO1 markedly rescues these CTS hypercontraction-induced suppressive phenotypes, which are analogous to those elicited by PIEZO1 hyperactivation. Consistently, PIEZO1 activation in murine hair follicle stem cells elevates intracellular calcium, triggering mitochondrial membrane permeabilization to release pro-apoptotic factors and ultimately induce apoptosis[67]; and PIEZO1-mediated calcium signaling also suppresses murine HFSC activation and impedes hair regeneration[83]. We conclude that the role of PIEZO1 in sensing the abnormal mechanical force from the microenvironment to regulate the HFSC apoptosis and proliferation is conserved across species, and the mechanosensitive channel might be a therapeutic target for hair loss. While our data support a conserved role for PIEZO1 in sensing aberrant mechanical cues within the follicular microenvironment, the downstream molecular pathways linking PIEZO1 hyperactivation to mitochondrial dysfunction, apoptosis, and cell-cycle arrest warrant further investigation.

Dihydrotestosterone (DHT), a potent androgen converted from testosterone via 5α-reductase, is recognized as a key contributor to AGA pathogenesis. Current evidence suggests that DHT binding to the androgen receptor (AR) in HFs triggers downstream events (e.g., inhibition of HF cell proliferation), leading to shortened anagen phase and progressive miniaturization[1–3]. However, the precise mechanisms by which DHT acts through AR—or whether DHT contributes to AGA via AR-independent pathways—remain incompletely defined. A recent seminal study revealed that DHT promotes muscle cell contraction by engaging the membrane receptor GPR133[65]. We now demonstrate that DHT not only induces CTS hypercontraction through GPR133 but also triggers progenitor cell apoptosis, suppresses proliferation in matrix and ORS cells, and ultimately inhibits hair growth. Notably, while AR blockade partially reverses DHT-mediated HF growth suppression, it fails to attenuate CTS contraction. These findings indicate two distinct mechanisms underpinning DHT's role in AGA: (1) canonical AR signaling in HF cells (e.g., DP and ORS cells), and (2) GPR133-dependent hypercontraction in CTS components (e.g., DS cells). This non-canonical DHT-GPR133 contractile axis might represent an important consideration for future therapeutics, particularly since AR-targeting strategies alone may not correct aberrant CTS dynamics.

Several limitations should be acknowledged. First, due to artifacts in scRNA-seq analyses introduced by enzymatic digestion, cell dispersion, capture rate disparities and representational bias, and loss of spatial context[84,85], as well as the limited number of human hair follicle samples available for sequencing, observed cellular/molecular alterations—particularly those occurring in rare cell types (e.g., DP cells) or loss of defined cell types (e.g., IRS cells) or involving interactions between different cell types—should be interpreted with caution in this study. Future spatial transcriptomic profiling of native occipital (non-balding) and frontotemporal (balding) scalp tissues from larger and independent AGA patient cohorts will be important to further validate and refine the transcriptional signatures identified here and to improve their generalizability. Second, this study provides no

https://doi.org/10.1038/s41467-026-70153-4

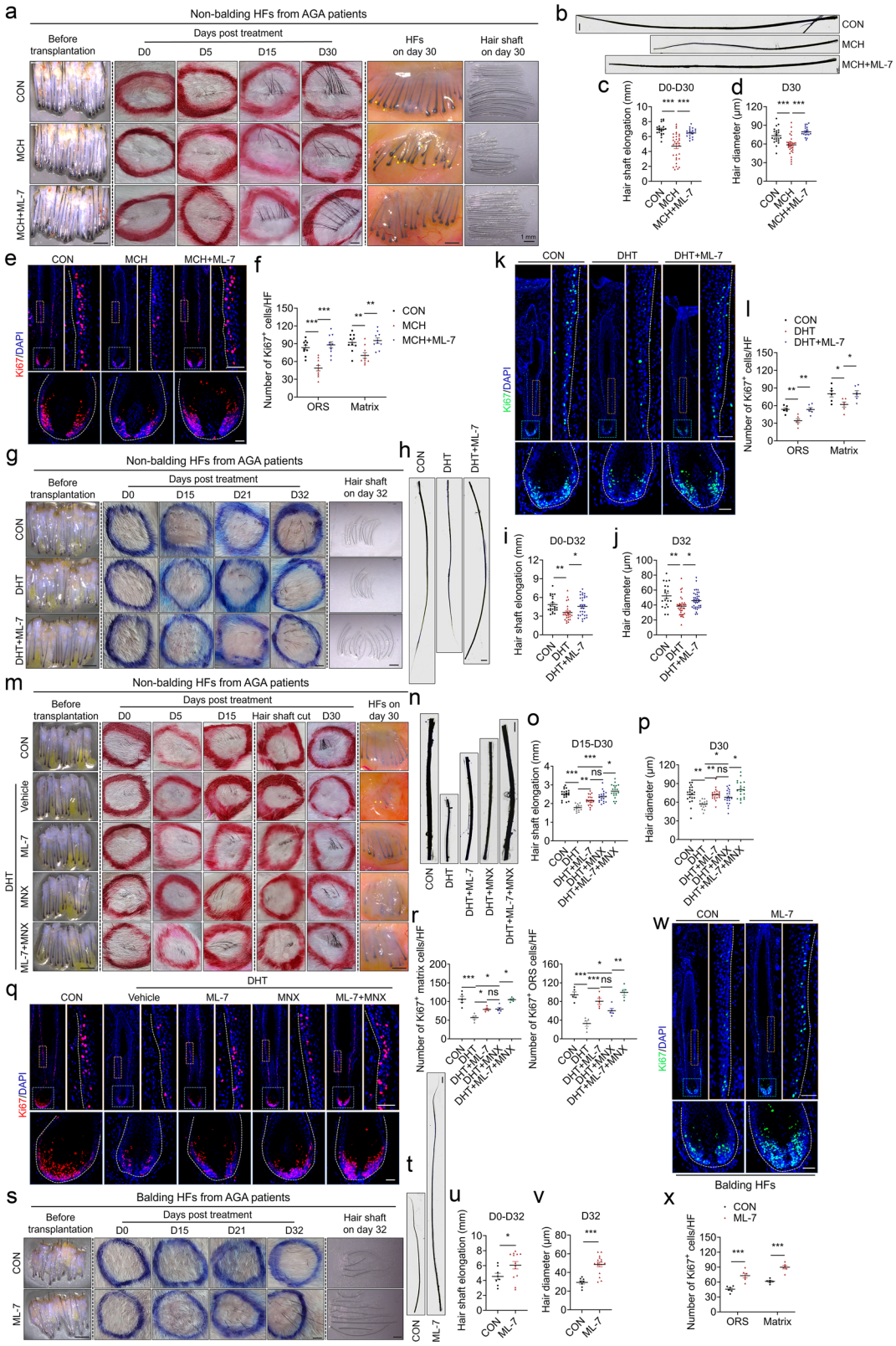

mechanistic evidence elucidating why aberrant CTS contraction exerts differential effects on spatially distinct ORS and matrix cells within human hair follicles. Specifically, aberrant CTS contraction simultaneously induces apoptosis and inhibits proliferation in ORS cells, whereas matrix cells exhibit only proliferation suppression at the early stage. We postulate that this heterogeneity may correlate with spatially varying magnitudes of mechanical forces generated by CTS contraction along the hair follicle. Future studies incorporating high-resolution biomechanical force mapping, compartment-specific mechano-transduction reporters, or localized mechanical perturbation strategies will be required to rigorously test this hypothesis. Third, as only male human samples were analyzed, potential sex-specific differences in CTS regulation and mechanotransduction remain to be addressed.

Fig. 6 | Inhibition of CTS contraction by ML-7 improves the growth of AGA patient-derived hair follicles in humanized mouse models. a, b Representative images of humanized mouse models engrafted with NB anagen HFs from AGA patients, showing HF growth before transplantation, during treatment, and after harvesting, and corresponding harvested hair shafts. **c, d** Quantification of hair shaft elongation and diameter following MCH and MLCK inhibitor treatment (n = 21/32/18 HFs from 2 AGA patients). **e, f** Immunostaining and quantification of Ki67-positive ORS and matrix cells in engrafted HFs (n = 10 HFs from 2 AGA patients per group). Right and bottom panels, magnified images of boxed areas. **g–l** Representative images and quantification of HF growth, hair shaft morphology, and epithelial proliferation following dihydrotestosterone (DHT) and MLCK inhibitor treatment (n = 22/25/30 HFs from 2 AGA patients). **m–r** Comparison of HF growth and epithelial proliferation following DHT treatment alone or combined with MLCK inhibitor or minoxidil (n = 20/15/20/20/20 HFs from 2 AGA patients). **s–x** Growth and proliferation analysis of B anagen HFs treated with MLCK inhibitor (n = 8/13 HFs from 2 AGA patients). Scale bars, 1 mm (**a**, **g**, **m**, **s**), 200 μm (**b**, **h**, **n**, **t**), 50 μm (**e**, **k**, **q**, **w**). Data are presented as means ± SEM. Statistical significance was assessed using one-way ANOVA with Tukey's post hoc test (**c**, **d**, **f**, **i**, **j**, **l**, **o**, **p**, **r**) and two-tailed unpaired Student's t test (**u**, **v**, **x**). P values are indicated in Source data file. $^{*}P < 0.05$, $^{**}P < 0.01$, $^{***}P < 0.001$, determined by ns, not significant.

In summary, the present study reveals the cellular hierarchies via spatial and single-cell transcriptomics analysis and demonstrates hyperactive CTS contraction as a critical cause of HF growth retardation in AGA, strongly suggesting that relaxing hair follicle by targeting CTS might be a promising therapy for this disorder.

Methods

Human scalp and HF samples

Human scalp skin biopsies and HF units were collected from non-balding occipital and balding frontal sites of male AGA patients undergoing hair transplantation surgery, and normal frontal sites of male healthy volunteers from the Department of Dermatology in Xiangya Hospital, Central South University. The detailed information for all specimens used in this study is listed in Supplementary Data 18, including patient/donor sources, biopsy sites, and respective methodologies. The procedures were in accordance with protocols set out in the WMA Declaration of Helsinki and the Department of Health and Human Services Belmont Report, and approved by the ethical committee of the Xiangya Hospital of Central South University (No. 202203076), and written informed consent was acquired from all participants.

Identification of hair cycle phases in human HFs

Hair cycle phases of human HFs were determined by morphological analysis, HE staining, co-immunostaining of Ki67 and TUNEL, immunostaining of Cleaved Caspase-3 (C-Caspase-3), and Hematoxylin staining for melanin content as previously described[41–43]. With these identification methods, or among the representative ones, all human HFs used in this study (including scRNA-seq, Stetro-seq, staining, in vitro organ culture and humanized mouse model) had been confirmed in the typical anagen phase before experimentation unless otherwise stated.

Preparation of single-cell suspensions of HF units

To obtain a single-cell suspension of entire HF units, DPs were isolated first by micro-dissection from HFs and were chopped. The remaining hair follicle tissue samples were cut with scissors and digested with the chopped DPs in 4 mg/ml Dispase II and Collagenase IV for 40 min at 37 °C, centrifuged at 200 × g for 5 min. The pellet was resuspended and digested in 0.25% trypsin for 10 min at 37 °C, washed in PBS + 5%FBS and filtered through a 70 μm cell strainer. The Dead Cell Removal Kit (Miltenyi Biotec) was used in accordance with the manufacturer's instruction to obtain live cells. 10 μL of the cell suspension were mixed with the same volume of Trypan blue for cell counting. The loading volume for sequencing was verified by the cell concentration

ScRNA-seq

scRNA-seq mainly includes GEM (gel bead-in-emulsion) generation, barcoding, cDNA amplification, library construction and sequencing. These steps were completed according to the user's instructions of Chromium Single Cell 3′ Reagent Kits v3.1 (10× Genomics, product code: 1000268, 1000215, 1000120) (https://www.10xgenomics.com/support/single-cell-gene-expression). Libraries were sequenced by an Illumina NovaSeq6000 System. Approximately 10,000 cells (targeting 5000–12,000) per sample were used for single-cell RNA sequencing.

ScRNA-seq data processing and cell type identification

We used the default parameters of Cell Ranger software suite (v6.0.2) to align and quantify the raw reads data from 10× Genomics. After the initial Cell Ranger metric assessment, Seurat (v4.3.0)[86] in R version 4.3.1 was used to exclude cells with fewer than 200 genes or more than 6000 genes detected, and more than 20% mitochondrial reads for downstream analysis.

After quality control, 76368 cells remained and were used for downstream bioinformatic analysis. The "NormalizeData" function was used to normalize the feature expression measurements for each cell by the total expression. The "ScaleData" function was used to scale and center the expression of each gene for dimensional reduction. To avoid batch effects among samples and experiments, we integrated data from all samples using harmony (v0.1.1). Total cell clustering was performed by "FindClusters"function with Louvain algorithm at a resolution of 0.2. Non-linear dimensional reduction was performed by "RunUMAP" function and visualized by Uniform Manifold Approximation and Projection (UMAP). Markers genes of each cell cluster were determined by "FindAllMarkers" function with Wilcoxon rank-sum test. Only those with |"avg_logFC"| ≥0.25 and "adjusted P value" ≤ 0.05 were considered as marker genes.

For subgroup cell clustering, cells of each cell type were extracted separately and clustered by their first 20 PCs and appropriate resolution. To further approximate the low-dimensional data manifold representing the differentiation trajectory for HFSCs, the spliced status of mRNAs in single-cell RNA sequencing data was used to estimations of RNA velocities through velocyto[87]. Markers genes of each subcluster were identified by "FindAllMarkers" function with the default parameters. "DoHeatmap" function were used to show top marker genes in heatmap.

Spatial transcriptomics analysis

Spatial transcriptomic profiling was performed using the Stereo-seq platform (BGI Genomics). Raw sequencing data were processed with the SAW pipeline (v8.1, https://github.com/STOmics/SAW) under default settings to align reads to the human reference genome. Gene expression matrix was subsequently normalized using the Stereopy package (Version 1.6.1, https://github.com/STOmics/stereopy). Cell-type identities were initially inferred by applying Cell2location[88], using single-cell RNA-seq–based annotations as a reference. We then performed unsupervised clustering using the "tl.spatial_neighbors" and the "tl.leiden" functions in the Stereopy package with the default parameters and refined the clusters by integrating spatial localization patterns and the expression of canonical marker genes. The final annotated dataset was converted into a Seurat object via the sceasy package (v0.0.7, https://github.com/cellgeni/sceasy), and marker gene expression across cell types was visualized using the DotPlot function.

Identification of balding-associated DEGs

We used the function of "FindMakers" in Seurat to identify balding-vs.-nonbalding and balding-vs.-healthy differentially expressed genes

(DEGs) for each cell type and sub-cell type. The adjusted *P* values of each DEG were calculated by non-parametric two-sided Wilcoxon rank-sum test and only those with |"avg_logFC"| > 0.25 and "adjusted *P* value" < 0.05 were to generate ranked gene lists for downstream Gene Set Enrichment Analysis (GSEA).

Function enrichment analysis

Gene Set Enrichment Analysis (GSEA) of GO and KEGG was performed by clusterProfiler R package (v4.5.1.902) and visualized with ggplot2 R package (v3.4.1)[89]. Representative terms selected from the top ranked GO terms and KEGG pathways from MsigDB were displayed.

Pseudotime analysis

To reconstruct the differentiation trajectory and do "branched expression analysis modeling" (BAEM) for HFSC fate cell determination related cell types, such as HFSCs to HF lineage and IFE lineage/sebaceous gland cells, Monocle2[90] was used to reconstruct the differentiation trajectory for small set of cell types and "BAEM" function was performed to identify cell determination related molecules.

Cell–cell communication analysis

To assess cell–cell communications among different cell types, we used cellchat (v1.1.3) to infer the intercellular communication network from single-cell RNA-seq data. Only cell types with more than 10 cells were considered in the analysis. The "trimean" method is used for calculating the average gene expression per cell group in "computeCommunProb" function. Pairwise comparison and visualization are performed by cellchat build-in function, only interactions with *P* value lower than 0.05 are considered to be real.

HF organ culture

Human HFs were obtained from the non-balding occipital sites (unless stated otherwise) of male AGA patients undergoing hair transplantation surgery. After microdissection, the HFs were first incubated in William'E medium (ThermoFisher) for 24 h to re-equilibrate. HFs in anagen VI phase were randomly assigned to the different experimental groups. HFs were cultured at 37 °C with 5% CO_2 in WEM supplemented with 2 mM of L-glutamine, 10 ng/ml hydrocortisone, 10 μg/ml insulin and 1% penicillin/streptomycin mixure, and photographed under a stereoscope every two days to count hair shaft length and hair cycle stage. The hair cycle stage (anagen/early-catagen/mid-catagen) of HFs was determined according to the identification methods described above[41,42].

Humanized mouse model

All animals used in this study were bred and housed in individually ventilated cages in specific pathogen-free holdings with temperature and light control (12 h light and dark cycle). All animal experiments were carried out under the approval of and guidelines of the ethical committee of the Xiangya Hospital of Central South University (No. 2022020197). The humanized mouse model was established with slight modifications to existing protocols[26,72]. Anagen-stage HFs from the occipital (non-balding) and frontal (balding) scalp regions of male AGA patients were implanted into dorsal incisions of male SCID mice ($n = 10–20$ HFs per mouse) under isoflurane anesthesia. Starting on post-grafting day 30, the mice received treatments of MCH (1 mM), ML-7 (100 μM), DHT (0.625 mg/mL), or Minoxidil (30 mg/mL), as indicated. Mice were sacrificed at day 30/32 post-treatment. HF morphology and hair shaft dimensions (length/diameter) were assessed using photomicroscopy and ImageJ analysis.

Chemical stimulation of HFs

All the chemicals were purchased from Selleck. After 24 h, medium was replaced and HFs were treated with vehicle (0.1% DMSO), MCH (0.1,1 10,100 μM as indicated), ML-7(0.3 μM), Z-VAD-FMK (10 μM), YODA1(15 μM), DHT (10 μM), RN17347 (3 μM), or GsMTX4(1 μM) according to the design of different experiments and the medium was changed daily with the indicated treatment. HFs were cultured for 2–10 days for analysis of hair growth and immunostaining.

Immunostaining and TUNEL staining. Immunostaining was performed as previously described[91]. Briefly, OCT-embedded samples were sectioned (10 μm) with a Leica cryostat. The sections were fixed for 10 min with 4% PFA, and washed with PBS, then blocked for 60 min with blocking buffer (5% NDS, 1% BSA, 0.3% Triton X-100). Primary antibodies were incubated overnight at 4 °C. Secondary antibody was incubated for 60 min at room temperature. After washed, sections were counterstained with DAPI. TUENL staining was performed with TUNEL assay kit (Roche, USA) according to manufacturer's instructions, and then stained with CD34 following the immunostaining protocol. For the co-immunostaining of two antibodies from the same host species, double immunohistochemistry for paraffin sections (8 μm) was conducted by using the Opal 4 color manual immunohistochemistry (IHC) kit (NEL810001KT, PerkinElmer). The signal of p-MLC2 was amplified by the Opal 4 color manual IHC kit (NEL810001KT, PerkinElmer). All pictures were taken with a Zeiss Axioplan 2 microscope. The fluorescence intensity was evaluated with ImageJ. The primary antibodies were used in this study: Rabbit anti-SOX9 (1:100, Cell Signaling), Mouse anti-KRT15 (1:2000, Lab vision), Mouse anti-KRT14 (1:4000, Abcam), Rabbit anti-KRT6A (1:500, Atlas Antibodies), Rabbit anti-KRT10 (1:1000, Abcam), Mouse anti-α-SMA (1:4000, Abcam), Rabbit anti-CD200 (1:200, Cell Signaling), Rabbit anti-CD34 (1:250, Abcam), Rabbit anti-Cleaved Caspase-3 (1:400, Cell Signaling), Rabbit anti-p-MLC2 (1:100, Cell Signaling), Rabbit anti-Ki67 (1:500, Abcam), Rabbit anti-PIEZO1 (1:100, Proteintech), Rabbit anti-EDNRA (1:500, Abcam), Rabbit anti-GPR133 (1:100, Novus), Rabbit anti-CCN2 (1:100, Proteintech), Rabbit anti-AR(1:100, Cell Signaling). Staining intensity was evaluated in well-defined reference by quantitative (immuno-) histomorphometry using NIH ImageJ software.

Isolation and culture of primary human DS cells

Non-balding and balding human HFs from the same AGA patient were micro-dissected under sterile conditions using fine forceps and microscissors. Adipose tissue and supra-sebaceous segments were meticulously removed under microscopic guidance. Isolated HFs were enzymatically treated with 1 mg/mL dispase II in Hanks' balanced salt solution for 1 h at 37 °C to separate the dermal sheath from the epithelial component. The liberated dermal sheath tissue was then transferred to a solution containing 2 mg/mL collagenase type IV and incubated for 1 h at 37 °C with periodic agitation. The digested suspension was dissociated by gentle pipetting and immediately quenched with DMEM supplemented with 5% fetal bovine serum. The cell suspension was sequentially filtered through a 40-μm cell strainer and centrifuged at 500 g for 10 min at 4 °C. The pelleted cells were resuspended in growth medium consisting of DMEM/F12 with 10% FBS and 1% penicillin-streptomycin. Cells were seeded onto tissue culture plates pre-coated with 50 μg/mL rat tail collagen type I and maintained at 37 °C in a humidified 5% CO_2 incubator. Medium changes were performed every 72 h until 80% confluency, with subsequent passages using 0.25% trypsin-EDTA. Primary cells between passages 2–4 were utilized for experiments.

In vitro Ca^{2+} imaging

HFs were incubated with Calbryte™ 520 AM fluorescent calcium indicator (AAT Bioquest) in culture medium at 37 °C for 1 h. Afterward HFs were washed with HBSS and cultured with HBSS supplemented with 1 mM calcium. For different treatments, MCH, ML-7, YODA1 or GsMTX4 was added to the culture medium for 30 min. The HFs were embedded in OCT and were sectioned with a Leica cryostat. Images were taken immediately to record the fluorescence intensity to

indicate Ca^{2+} concentration and the adjacent section was used for CD34 staining to indicate progenitor cells.

Atomic force microscopy (AFM) for cell stiffness measurement

Primary human DS cells were seeded at a density of 5×10^3 cells/cm^2 on sterile 35-mm Petri dishes pre-coated with collagen type I (5 μg/cm^2) and allowed to adhere for 24 h before AFM analysis. Stiffness measurements were performed using a JPK Nanowizard IV AFM system coupled with an inverted optical microscope (Nikon Eclipse Ti2) as previously described[83]. Cells were maintained in 1× phosphate-buffered saline (PBS) at 37 °C during measurements. A cylindrical nitride cantilever (Bruker SAA-SPH-5UM; tip radius: 5 μm, spring constant: 0.20–0.30 N/m) was used for all experiments. The cantilever's spring constant was calibrated before each experiment via the thermal fluctuation method. Indentations were performed at a constant approach rate of 5 μm/s with a maximum cantilever deflection set point of 2.0 nN to ensure elastic-dominant deformation. Force-indentation curves were recorded at 5 points over the perinuclear region of individual cells (≥6 cells per group).

Young's modulus (E) was derived by fitting the approaching force curve to the Hertzian contact model for a spherical indenter (Eq. 1):

$$F(x) = \frac{4}{3} \cdot \frac{E}{1 - u^2} \sqrt{r} x^{3/2}$$

where F = applied force, r = tip radius (5 μm), δ = indentation depth, and υ = Poisson's ratio (fixed at 0.5 based on biological soft materials). Baseline correction and contact point estimation were automated using JPK Data Processing Software (v6.3). Cells with excessive drift or incomplete retraction curves were excluded.

Ex vivo hair follicle and DS cell contraction assays

Human HFs were micro-dissected from scalp tissue, approved by the ethical committee of the Xiangya Hospital of Central South University (No. 202203076) and written informed consent was acquired from all participants. HFs underwent 60 min equilibration at 37 °C in glucose-supplemented HBSS ± 1 μM ML-7. Real-time imaging used a Leica TCS SP8 confocal system (10× air objective, 37 °C, 5% CO_2). Immediately prior to time-lapse imaging, the buffer was replaced with HBSS containing 1 mM $CaCl_2$ supplemented with or without contraction inducers (10 μM DHT or MCH). Brightfield images were acquired at 5-min intervals for 15 min. Primary DS cells isolated from matched follicles were cultured on collagen I-coated 24-well plate. After identical pre-treatment, induction buffers were replaced simultaneously with HF experiments. Phase-contrast imaging proceeded for 30 min at 10-min intervals. HF diameter was measured perpendicular to the axis at five locations (200-400 μm superior to dermal papilla, 50 μm intervals) using Fiji/ImageJ v.2.3.0. Cell area was quantified via automated thresholding.

ACH content quantification

ACH levels in serum and HFs were measured using an ACH assay kit (Catalog No. A105-1-1 for HFs, A105-2-1 for serum, Nanjing Jiancheng Bioengineering Institute) according to the manufacturer's instructions.

Detection of cell apoptosis using Annexin V-FITC assay kit

Cell apoptosis was detected using the Annexin V-FITC Apoptosis Detection Kit (ThermoFisher). Cells were resuspended in binding buffer (1×10^6 cells/mL) and incubated with 5 μL Annexin V-FITC and 5 μL propidium iodide (PI) for 15 min at room temperature in the dark. After adding 400 μL of binding buffer, cells were analyzed by flow cytometry. Early apoptotic cells were Annexin V-FITC-positive, PI-negative, while late apoptotic or necrotic cells were both Annexin V-FITC and PI-positive.

Isolation and culture of primary human ORS cells

Outer root sheath (ORS) cells were isolated from hair follicles (HFs) of AGA patients using previously described methods (PMID: 40776528). HFs were harvested and digested with 0.1% dispase (Sigma, USA) at 37 °C for 1 h. The connective tissue sheath (CTS) was carefully removed under a stereomicroscope to expose the ORS. The ORS was then dissociated into single cells by incubation with 0.05% trypsin (Gibco, USA) at 37 °C for 30 min. The resulting cell suspension was vortexed and filtered through a 40 μm cell strainer (Falcon, USA) to remove debris. Cells were then centrifuged at 300 × g for 5 min, resuspended in culture medium, and seeded onto culture plates pre-coated with 10 μg/mL human fibronectin (Sigma, USA). The plates were incubated at 37 °C for 1 h, and non-adherent cells were removed by changing the culture medium. ORS cells were cultured in CNT-07 medium (CELLNTEC, Switzerland) at 37 °C with 5% CO_2. The culture medium was replaced every 2 days.

Detection of mitochondrial function

Mitochondrial function in ORS cells was assessed using the JC-1 Mitochondrial Membrane Potential Kit (Beyotime). Cells were incubated with 2 μM JC-1 at 37 °C for 20 min, then washed and analyzed by fluorescence microscopy. Red fluorescence indicates high mitochondrial membrane potential, while green fluorescence indicates depolarization. An increase in the green-to-red fluorescence ratio suggests increased mitochondrial permeability, a sign of mitochondrial dysfunction.

Immunoblotting

Cells were lysed in RIPA buffer (ThermoFisher) containing protease inhibitors (ThermoFisher) after being washed with cold PBS. The proteins were quantified via bicinchoninic acid assay (ThermoFisher) and separated on SDS-PAGE and transferred to a PVDF membrane. The membrane was blocked with 5% nonfat milk for 1 h at room temperature and incubated with primary antibodies overnight at 4 °C. The secondary antibodies HRP-conjugated Goat anti-Mouse IgG (Santa Cruz) and HRP-conjugated Goat anti-Rabbit IgG secondary antibody (Santa Cruz) were incubated for 1 h at room temperature. The immunoreactive bands were visualized by the HRP substrate (Sigma) on ChemiDoc XRS+ system (Bio-Rad). Data were analyzed by GE Healthcare ImageQuant LAS 4000 Mini and images have been cropped for presentation. The corresponding uncropped images of immunoblotting results were provided in the Resource data file. The primary antibodies used in this study were: Rabbit anti-p-MLC2 (1:1000, Cell Signaling), Rabbit anti MLC2 (1:2000, Proteintech), Rabbit anti-GPR133 (1:1000, Novus), Rabbit anti cleaved-CASPASE3(1:1000, Cell Signaling), Mouse anti GAPDH (1:10000, Proteintech).

RNA interference

Small interferring RNA (siRNA) were purchased from GenePharma (China). The sequences for siRNA: sih*GPR133*: CCAGGCCAAGTGTTATGAGAA; sih*AR*: CACCAATGTCAACTCCAGGAT; ORS cells were transfected with siRNA at 0.06 nM packaged by Lipofectamine 3000 (Invitrogen) in 6-well plates (5×10^5cells/well). Hair follicles were transfected with siRNA at 0.06 nM packaged by Lipofectamine 3000 (Invitrogen) in 24-well plates (1 hair follicle/well).

EdU proliferation assay. Cell proliferation was evaluated using the EdU Cell Proliferation Assay kit (RiboBio). ORS cells were cultured in medium with YODA1 as indicated. After 24 h of incubation in medium containing 10 μM EdU, cells were fixed with 4% paraformaldehyde. Subsequently, cell nuclei were stained with DAPI to facilitate visualization. EdU-positive cells, indicative of DNA synthesis, were quantified using fluorescence microscopy. The proportion of EdU-incorporating cells was calculated relative to the total cell population.

RNA extraction, real-time PCR (qPCR)

RNA was extracted from the bulbs of human hair follicles using TRIzol Reagent (ThermoFisher) and was reverse-transcribed to cDNA by PrimeScript™ RT reagent Kit with gDNA Eraser (Takara). qPCR was performed with ChamQ Universal SYBR qPCR Master Mix (Vazyme). The relative gene expression was measured by delta-delta CT relative to GAPDH, and the fold change was normalized to the control group. The primer sequences used in this study were presented in Supplementary Data 19.

Statistical analysis

All data were expressed as mean ± SEM and were analyzed by ANOVA or Kruskall–Wallis test when more than two groups were compared or Student's t-test when only two groups were compared. Graphpad Prism 10, R (v4.1.3) and Excel (Microsoft) were used to assess statistical significance. Statistical significance was set at a $P < 0.05$. *, ** and *** indicate $P < 0.05$, $P < 0.01$ and $P < 0.001$, respectively. All corresponding P values are listed in the Source data file.

Reporting summary

Further information on research design is available in the Nature Portfolio Reporting Summary linked to this article.

Data availability

All data needed to assess the conclusions in the present study are provided in the manuscript and/or the Supplementary Materials. The scRNA-seq and Stereo-seq datasets are available from the genome sequence archive under accession number HRA005629 and HRA012638, respectively (http://bigd.big.ac.cn/gsa-human/). Any other data supporting the findings of this study are available from the corresponding author upon reasonable request. Source data are provided as a source data file. Source data are provided with this paper.

References

1. Cuevas-Diaz Duran, R. et al. The biology and genomics of human hair follicles: a focus on androgenetic alopecia. *Int. J. Mol. Sci.* **25**, 2542 (2024).
2. Sinclair, R., Torkamani, N. & Jones, L. Androgenetic alopecia: new insights into the pathogenesis and mechanism of hair loss. *F1000Research* **4**, 585 (2015).
3. Inui, S. & Itami, S. Molecular basis of androgenetic alopecia: from androgen to paracrine mediators through dermal papilla. *J. Dermatol. Sci.* **61**, 1–6 (2011).
4. Altendorf, S., Bertolini, M., Le Riche, A., Tosti, A. & Paus, R. Frontiers in the physiology of male pattern androgenetic alopecia: beyond the androgen horizon. *Physiol. Rev.* **106**, 121–195 (2026).
5. Liu, Y. et al. Androgenetic alopecia. *Nat. Rev. Dis. Primers* **11**, 73 (2025).
6. Lolli, F. et al. Androgenetic alopecia: a review. *Endocrine* **57**, 9–17 (2017).
7. Ntshingila, S., Oputu, O., Arowolo, A. T. & Khumalo, N. P. Androgenetic alopecia: an update. *JAAD Int.* **13**, 150–158 (2023).
8. Huang, C. H., Fu, Y. & Chi, C. C. Health-related quality of life, depression, and self-esteem in patients with androgenetic alopecia: a systematic review and meta-analysis. *JAMA Dermatol.* **157**, 963–970 (2021).
9. Russo, P. M. et al. HrQoL in hair loss-affected patients with alopecia areata, androgenetic alopecia and telogen effluvium: the role of personality traits and psychosocial anxiety. *J. Eur. Acad. Dermatol. Venereol.* **33**, 608–611 (2019).
10. Cash, T. F. The psychosocial consequences of androgenetic alopecia: a review of the research literature. *Br. J. Dermatol.* **141**, 398–405 (1999).
11. Wang, X. et al. Psychological assessment in 355 Chinese college students with androgenetic alopecia. *Medicine* **97**, e11315 (2018).
12. Hadshiew, I. M., Foitzik, K., Arck, P. C. & Paus, R. Burden of hair loss: stress and the underestimated psychosocial impact of telogen effluvium and androgenetic alopecia. *J. Investig. Dermatol.* **123**, 455–457 (2004).
13. Katzer, T., Leite Junior, A., Beck, R. & da Silva, C. Physiopathology and current treatments of androgenetic alopecia: going beyond androgens and anti-androgens. *Dermatol. Ther.* **32**, e13059 (2019).
14. Adil, A. & Godwin, M. The effectiveness of treatments for androgenetic alopecia: a systematic review and meta-analysis. *J. Am. Acad. Dermatol.* **77**, 136–141.e135 (2017).
15. Diviccaro, S., Melcangi, R. C. & Giatti, S. Post-finasteride syndrome: an emerging clinical problem. *Neurobiol. Stress* **12**, 100209 (2020).
16. Nestor, M. S., Ablon, G., Gade, A., Han, H. & Fischer, D. L. Treatment options for androgenetic alopecia: efficacy, side effects, compliance, financial considerations, and ethics. *J. Cosmet. Dermatol.* **20**, 3759–3781 (2021).
17. Motofei, I. G. et al. Androgenetic alopecia; drug safety and therapeutic strategies. *Expert Opin. Drug Saf.* **17**, 407–412 (2018).
18. Heilmann-Heimbach, S., Hochfeld, L. M., Paus, R. & Nothen, M. M. Hunting the genes in male-pattern alopecia: how important are they, how close are we and what will they tell us? *Exp. Dermatol.* **25**, 251–257 (2016).
19. Deng, Z. et al. Androgen receptor-mediated paracrine signaling induces regression of blood vessels in the dermal papilla in androgenetic alopecia. *J. Investig. Dermatol.* **142**, 2088–2099 e2089 (2022).
20. Devjani, S., Ezemma, O., Kelley, K. J., Stratton, E. & Senna, M. Androgenetic alopecia: therapy update. *Drugs* **83**, 701–715 (2023).
21. Deng, Z. et al. mTOR signaling promotes stem cell activation via counterbalancing BMP-mediated suppression during hair regeneration. *J. Mol. Cell Biol.* **7**, 62–72 (2015).
22. Muller-Rover, S. et al. A comprehensive guide for the accurate classification of murine hair follicles in distinct hair cycle stages. *J. Investig. Dermatol.* **117**, 3–15 (2001).
23. Greco, V. et al. A two-step mechanism for stem cell activation during hair regeneration. *Cell Stem Cell* **4**, 155–169 (2009).
24. Whiting, D. A. Possible mechanisms of miniaturization during androgenetic alopecia or pattern hair loss. *J. Am. Acad. Dermatol.* **45**, S81–S86 (2001).
25. Asfour, L., Cranwell, W. & Sinclair, R. Male Androgenetic Alopecia. In Endotext (eds Feingold, K. R. et al.) (South Dartmouth (MA): MDText.com, Inc., 2000).
26. Gilhar, A., Keren, A., Ullmann, Y., Wu, J. & Paus, R. Effect of minoxidil formulations on human scalp skin xenotransplants on SCID mice: a novel pre-clinical in vivo assay for androgenetic alopecia research. *Exp. Dermatol.* **31**, 980–982 (2022).
27. Plikus, M. V. & Chuong, C. M. Macroenvironmental regulation of hair cycling and collective regenerative behavior. *Cold Spring Harb. Perspect. Med.* **4**, a015198 (2014).
28. Morgan, B. A. The dermal papilla: an instructive niche for epithelial stem and progenitor cells in development and regeneration of the hair follicle. *Cold Spring Harb. Perspect. Med.* **4**, a015180 (2014).
29. Heitman, N. et al. Dermal sheath contraction powers stem cell niche relocation during hair cycle regression. *Science* **367**, 161–166 (2020).
30. Festa, E. et al. Adipocyte lineage cells contribute to the skin stem cell niche to drive hair cycling. *Cell* **146**, 761–771 (2011).
31. Chen, D. et al. Fibroblast bioelectric signaling drives hair growth. *Cell* **188**, 5175–5193.e5121 (2025).
32. Tai, K. Y. et al. Adipocyte lipolysis activates epithelial stem cells for hair regeneration through fatty acid metabolic signaling. *Cell Metab.* **37**, 2202–2219.e2208 (2025).
33. Garza, L. A. et al. Bald scalp in men with androgenetic alopecia retains hair follicle stem cells but lacks CD200-rich and CD34-

positive hair follicle progenitor cells. *J. Clin. Investig.* **121**, 613–622 (2011).
34. Purba, T. S. et al. Divergent proliferation patterns of distinct human hair follicle epithelial progenitor niches in situ and their differential responsiveness to prostaglandin D2. *Sci. Rep.* **7**, 15197 (2017).
35. Ntshingila, S., Khumalo, N. P., Engel, M. & Arowolo, A. T. An appraisal of laboratory models of androgenetic alopecia: a systematic review. *Ski. Health Dis.* **1**, e15 (2021).
36. Deutsch, A., McLellan, B. N. & Shinoda, K. Single-cell transcriptomics in dermatology. *JAAD Int.* **1**, 182–188 (2020).
37. Mereu, E. et al. Benchmarking single-cell RNA-sequencing protocols for cell atlas projects. *Nat. Biotechnol.* **38**, 747–755 (2020).
38. Papalexi, E. & Satija, R. Single-cell RNA sequencing to explore immune cell heterogeneity. *Nat. Rev. Immunol.* **18**, 35–45 (2018).
39. Potter, S. S. Single-cell RNA sequencing for the study of development, physiology and disease. *Nat. Rev. Nephrol.* **14**, 479–492 (2018).
40. Jin, S. et al. Inference and analysis of cell-cell communication using CellChat. *Nat. Commun.* **12**, 1088 (2021).
41. Oh, J. W. et al. A guide to studying human hair follicle cycling in vivo. *J. Investig. Dermatol.* **136**, 34–44 (2016).
42. Langan, E. A., Philpott, M. P., Kloepper, J. E. & Paus, R. Human hair follicle organ culture: theory, application and perspectives. *Exp. Dermatol.* **24**, 903–911 (2015).
43. Kloepper, J. E. et al. Methods in hair research: how to objectively distinguish between anagen and catagen in human hair follicle organ culture. *Exp. Dermatol.* **19**, 305–312 (2010).
44. Zou, Z. et al. A single-cell transcriptomic atlas of human skin aging. *Dev. Cell* **56**, 383–397 e388 (2021).
45. Takahashi, R. et al. Defining transcriptional signatures of human hair follicle cell states. *J. Investig. Dermatol.* **140**, 764–773.e764 (2020).
46. Wu, S. et al. Single-cell transcriptomics reveals lineage trajectory of human scalp hair follicle and informs mechanisms of hair graying. *Cell Discov.* **8**, 49 (2022).
47. He, H. et al. Single-cell transcriptome analysis of human skin identifies novel fibroblast subpopulation and enrichment of immune subsets in atopic dermatitis. *J. Allergy Clin. Immunol.* **145**, 1615–1628 (2020).
48. Joost, S. et al. Single-cell transcriptomics of traced epidermal and hair follicle stem cells reveals rapid adaptations during wound healing. *Cell Rep.* **25**, 585–597.e587 (2018).
49. Rahmani, W. et al. Hair follicle dermal stem cells regenerate the dermal sheath, repopulate the dermal papilla, and modulate hair type. *Dev. Cell* **31**, 543–558 (2014).
50. Joost, S. et al. The molecular anatomy of mouse skin during hair growth and rest. *Cell Stem Cell* **26**, 441–457.e447 (2020).
51. Liu, X. et al. Single-cell RNA-sequencing reveals lineage-specific regulatory changes of fibroblasts and vascular endothelial cells in keloids. *J. Investig. Dermatol.* **142**, 124–135.e111 (2022).
52. Hughes, T. K. et al. Second-strand synthesis-based massively parallel scRNA-seq reveals cellular states and molecular features of human inflammatory skin pathologies. *Immunity* **53**, 878–894.e877 (2020).
53. Cui, C. Y. & Schlessinger, D. Eccrine sweat gland development and sweat secretion. *Exp. Dermatol.* **24**, 644–650 (2015).
54. Joost, S. et al. Single-cell transcriptomics reveals that differentiation and spatial signatures shape epidermal and hair follicle heterogeneity. *Cell Syst.* **3**, 221–237.e229 (2016).
55. Yang, H., Adam, R. C., Ge, Y., Hua, Z. L. & Fuchs, E. Epithelial-mesenchymal micro-niches govern stem cell lineage choices. *Cell* **169**, 483–496.e413 (2017).
56. Ghorbanalipoor, S. et al. The loss of keratin 77 in murine skin is functionally compensated by keratin 1. *Biochim. Biophys. Acta Mol. Cell Res.* **1872**, 119881 (2025).
57. Martino, P. A., Heitman, N. & Rendl, M. The dermal sheath: an emerging component of the hair follicle stem cell niche. *Exp. Dermatol.* **30**, 512–521 (2021).
58. Matsumura, H. et al. Hair follicle aging is driven by transepidermal elimination of stem cells via COL17A1 proteolysis. *Science* **351**, aad4395 (2016).
59. Morinaga, H. et al. Obesity accelerates hair thinning by stem cell-centric converging mechanisms. *Nature* **595**, 266–271 (2021).
60. Nayak, A. et al. Single-molecule analysis reveals that regulatory light chains fine-tune skeletal myosin II function. *J. Biol. Chem.* **295**, 7046–7059 (2020).
61. Huang, F. et al. Calcium-activated chloride channel TMEM16A modulates mucin secretion and airway smooth muscle contraction. *Proc. Natl. Acad. Sci. USA* **109**, 16354–16359 (2012).
62. Kudo, M. et al. IL-17A produced by alphabeta T cells drives airway hyper-responsiveness in mice and enhances mouse and human airway smooth muscle contraction. *Nat. Med.* **18**, 547–554 (2012).
63. Coates, A.L. et al. ERS technical standard on bronchial challenge testing: general considerations and performance of methacholine challenge tests. *Eur. Respir. J.* **49**, 1601526 (2017).
64. Colgren, J. & Nichols, S. A. MRTF specifies a muscle-like contractile module in Porifera. *Nat. Commun.* **13**, 4134 (2022).
65. Yang, Z. et al. Identification, structure, and agonist design of an androgen membrane receptor. *Cell* **188**, 1589–1604.e1524 (2025).
66. Li, X. et al. The caspase inhibitor Z-VAD-FMK alleviates endotoxic shock via inducing macrophages necroptosis and promoting MDSCs-mediated inhibition of macrophages activation. *Front. Immunol.* **10**, 1824 (2019).
67. Xie, Y. et al. Hair shaft miniaturization causes stem cell depletion through mechanosensory signals mediated by a Piezo1-calcium-TNF-alpha axis. *Cell Stem Cell* **29**, 70–85.e76 (2022).
68. Kefauver, J. M., Ward, A. B. & Patapoutian, A. Discoveries in structure and physiology of mechanically activated ion channels. *Nature* **587**, 567–576 (2020).
69. Ranade, S. S., Syeda, R. & Patapoutian, A. Mechanically activated ion channels. *Neuron* **87**, 1162–1179 (2015).
70. Tada, M., Takeuchi, A., Hashizume, M., Kitamura, K. & Kano, M. A highly sensitive fluorescent indicator dye for calcium imaging of neural activity in vitro and in vivo. *Eur. J. Neurosci.* **39**, 1720–1728 (2014).
71. Vincent, F. et al. Identification and characterization of novel TRPV4 modulators. *Biochem. Biophys. Res. Commun.* **389**, 490–494 (2009).
72. Gilhar, A., Keren, A. & Paus, R. Vellus-to-terminal hair follicle reconversion occurs in male pattern balding and is promoted by minoxidil and platelet-rich plasma: in vivo evidence from a new humanized mouse model of androgenetic alopecia. *Acta Derm. Venereol.* **103**, adv12320 (2023).
73. Zeltzer, A. A., Keren, A., Paus, R. & Gilhar, A. Topical minoxidil rejuvenates hair follicles from men with androgenetic alopecia in vivo. *Acta Derm. Venereol.* **104**, adv24213 (2024).
74. Driskell, R. R., Clavel, C., Rendl, M. & Watt, F. M. Hair follicle dermal papilla cells at a glance. *J. Cell Sci.* **124**, 1179–1182 (2011).
75. Chen, C. L., Huang, W. Y., Wang, E. H. C., Tai, K. Y. & Lin, S. J. Functional complexity of hair follicle stem cell niche and therapeutic targeting of niche dysfunction for hair regeneration. *J. Biomed. Sci.* **27**, 43 (2020).
76. Martel, J. L., Miao, J. H., Badri, T. & Fakoya, A. O. Anatomy, Hair Follicle. In StatPearls (Treasure Island (FL): StatPearls Publishing, 2025).
77. Plikus, M. V. New activators and inhibitors in the hair cycle clock: targeting stem cells' state of competence. *J. Investig. Dermatol* **132**, 1321–1324 (2012).

78. Jaworsky, C., Kligman, A. M. & Murphy, G. F. Characterization of inflammatory infiltrates in male pattern alopecia: implications for pathogenesis. *Br. J. Dermatol.* **127**, 239–246 (1992).
79. Peyravian, N., Deo, S., Daunert, S. & Jimenez, J. J. The inflammatory aspect of male and female pattern hair loss. *J. Inflamm. Res.* **13**, 879–881 (2020).
80. Magro, C. M., Rossi, A., Poe, J., Manhas-Bhutani, S. & Sadick, N. The role of inflammation and immunity in the pathogenesis of androgenetic alopecia. *J. Drugs Dermatol.* **10**, 1404–1411 (2011).
81. Martinez-Jacobo, L., Villarreal-Villarreal, C. D., Ortiz-Lopez, R., Ocampo-Candiani, J. & Rojas-Martinez, A. Genetic and molecular aspects of androgenetic alopecia. *Indian J. Dermatol. Venereol. Leprol.* **84**, 263–268 (2018).
82. Martino, P. et al. Progenitor-derived endothelin controls dermal sheath contraction for hair follicle regression. *Nat. Cell Biol.* **25**, 222–234 (2023).
83. Wang, J. et al. PIEZO1-mediated calcium signaling reinforces mechanical properties of hair follicle stem cells to promote quiescence. *Sci. Adv.* **11**, eadt2771 (2025).
84. Kharchenko, P. V. The triumphs and limitations of computational methods for scRNA-seq. *Nat. Methods* **18**, 723–732 (2021).
85. Weber, C. Single-cell spatial transcriptomics. *Nat. Cell Biol.* **23**, 1108 (2021).
86. Hao, Y. et al. Integrated analysis of multimodal single-cell data. *Cell* **184**, 3573–3587.e3529 (2021).
87. La Manno, G. et al. RNA velocity of single cells. *Nature* **560**, 494–498 (2018).
88. Kleshchevnikov, V. et al. Cell2location maps fine-grained cell types in spatial transcriptomics. *Nat. Biotechnol.* **40**, 661–671 (2022).
89. Bechhofer, D. H., Kornacki, J. A., Firshein, W. & Figurski, D. H. Gene control in broad host range plasmid RK2: expression, polypeptide product, and multiple regulatory functions of korB. *Proc. Natl. Acad. Sci. USA* **83**, 394–398 (1986).
90. Qiu, X. et al. Reversed graph embedding resolves complex single-cell trajectories. *Nat. Methods* **14**, 979–982 (2017).
91. Deng, Z. et al. A positive feedback loop between mTORC1 and cathelicidin promotes skin inflammation in rosacea. *EMBO Mol. Med.* **13**, e13560 (2021).

Acknowledgements

This work was supported by the National Natural Science Funds for Distinguished Young Scholars (No. 82225039), the National Natural Science Funds for Excellent Young Scientists (No. 82422063), Postdoctoral Fellowship Program of CPSF (No. BX20230435), the National Key Research and Development Program of China (No. 2023YFC2509003), the National Natural Science Foundation of China (No. 82304057, No. 82173448, No. 82373508, No. 82303992, No. 82373509, No. 82574005), the Natural Science Funds of Hunan province for excellent Young Scholars (No. 2023JJ20094), the Natural Science Foundation of Hunan Province, China (No. 2021JJ31079, No. 2023JJ30940), Educational Science Planning Project of Hunan Province (No. ND206997). This work was carried out in part using hardware and/or software provided by the Center for Computational Biology and Bioinformatics, Furong Laboratory and Bioinformatics Center, Xiangya Hospital, Central South University. We thank our colleagues (Department of Dermatology, Xiangya Hospital, Central South University, China) for their generous support throughout this work.

Author contributions

J.L., Z.D., G.L., L.Y., and Y.T. designed and conceived the study. Z.D., G.L., and L.Y. performed data analyses. L.Y. and Z.D. performed scRNA-seq analysis. G.L., Z.D., S.D., and M.C. performed most experiments. Y.Z., F.L., Y.W., S.X., Z.W., B.W., Z.Z., M.W., J.Y.L., and W.S. contributed to sample collection. Z.D. and M.C. help to generate sequencing libraries. H.X., M.L., and Y.Z. provide critical discussion and suggestion. Z.D., G.L., L.Y., J.L., and Y.T. prepared the manuscript with input from coauthors.

Competing interests

The authors declare no competing interests.

Additional information

Supplementary information The online version contains supplementary material available at https://doi.org/10.1038/s41467-026-70153-4.

Correspondence and requests for materials should be addressed to Yan Tang, Zhili Deng or Ji Li.

Peer review information *Nature Communications* thanks the anonymous, reviewer(s) for their contribution to the peer review of this work. A peer review file is available.

Reprints and permissions information is available at http://www.nature.com/reprints

Publisher's note Springer Nature remains neutral with regard to jurisdictional claims in published maps and institutional affiliations.

[1]Department of Dermatology, Xiangya Hospital, Central South University, Changsha, Hunan, China. [2]Hunan Key Laboratory of Aging Biology, Xiangya Hospital, Central South University, Changsha, Hunan, China. [3]National Clinical Research Center for Geriatric Disorders, Xiangya Hospital, Central South University, Changsha, Hunan, China. [4]FuRong Laboratory, Changsha, China. [5]Department of Dermatology, The Second Hospital of Hunan University of Chinese Medicine, Changsha, Hunan, China. [6]Department of Dermatology, Second Affiliated Hospital of Xinjiang Medical University, Urumqi, China. [7]Key Laboratory of Biorheological Science and Technology of Ministry of Education &111 Project Laboratory of Biomechanics and Tissue Repair, College of Bioengineering, Chongqing University, Chongqing, China. [8]These authors contributed equally: Guo Li, Li Yang, Shixin Duan. ✉e-mail: ytang_xy@csu.edu.cn; dengzhili@csu.edu.cn; liji_xy@csu.edu.cn